Turbulence in Core-collapse Supernovae

David Calvert[1] , Michael Redle[2,3] , Bibek Gautam[1] , Charles J. Stapleford[4] , Carla Fröhlich[1] , James P. Kneller[1] , and
Matthias Liebendorfer[5]

[1] Department of Physics, North Carolina State University, Raleigh, NC 27606, USA
[2] Department of Mathematics, North Carolina State University, Raleigh, NC 27606, USA
[3] Institute of Applied and Computational Mathematics, RWTH Aachen University, 52062 Aachen, Germany
[4] Oak Ridge National Laboratory, Oak Ridge, TN 37830, USA
[5] University of Basel, Basel, Switzerland

Abstract

It is understood in a general sense that turbulent fluid motion below the shock front in a core-collapse supernova stiffens the effective equation of state of the fluid and aids in the revival of the explosion. However, when one wishes to be precise and quantify the amount of turbulence in a supernova simulation, one immediately encounters the problem that turbulence is difficult to define and measure. Using the 3D magnetohydrodynamic code ELEPHANT, we study how different definitions of turbulence change one's conclusions about the amount of turbulence in a supernova and the extent to which it helps the explosion. We find that, while all the definitions of turbulence we use lead to a qualitatively similar growth pattern over time of the turbulent kinetic energy in the gain region, the total amount of turbulent kinetic energy, and especially the ratios of turbulent to total kinetic energy, distinguish them. Some of the definitions appear to indicate turbulence is a necessary contributor to the explosion, and others indicate it is not. The different definitions also produce turbulence maps with different correlations with maps of the enstrophy, a quantity widely regarded as also indicating the presence of turbulence. We also compute the turbulent adiabatic index and observe that, in regions of low enstrophy, this quantity is sensitive to the definition used. As a consequence, the effective adiabatic index depends upon the method used to measure the turbulence, and thus it alters one's conclusions regarding the impact of turbulence within the supernova.

Unified Astronomy Thesaurus concepts: Core-collapse supernovae (304); Supernova dynamics (1664); Computational astronomy (293)

1. Introduction

Core-collapse supernovae (CCSNe) are the explosive deaths of stars with initial masses greater than $\sim$8–10 $M_\odot$ (S. E. Woosley et al. 2002; S. J. Smartt et al. 2009; S. E. Woosley & A. Heger 2015). In addition to the spectacular fireworks, nuclear reactions in the ejected material will contaminate the interstellar medium of the host galaxy with freshly synthesized elements (K. Nomoto et al. 2006; S. Curtis et al. 2019; L. Boccioli & L. Roberti 2024). Stellar-mass black holes, neutron stars, pulsars, and magnetars are born out of these explosions (A. Burrows & J. M. Lattimer 1986; R. C. Duncan & C. Thompson 1992; K. Nomoto et al. 2011; S. Mereghetti et al. 2015; V. M. Kaspi & A. M. Beloborodov 2017; L. J. Wang et al. 2017; K. Ebinger et al. 2019), and observations indicate that long gamma-ray bursts are also associated with CCSNe (J. S. Bloom et al. 1999; S. E. Woosley & J. S. Bloom 2006). Despite the importance of CCSNe in understanding many aspects of the Universe, the mechanism that drives CCSN explosions is not yet fully understood. At the present time, the prevailing theory for CCSNe is based upon the "delayed neutrino-heating mechanism" (H. A. Bethe & J. R. Wilson 1985; A. Burrows et al. 1995; H. T. Janka 2025). In this paradigm, an initial collapse of the stellar core forms a proto-neutron star (PNS) and launches a shockwave into the outer layers. The shock stalls 100–200 km

above the PNS as its energy is consumed, dissociating infalling nuclei, and it is then revived through energy deposition due to neutrino scattering/absorption in the material beneath the shock. However simulations of supernovae in spherical symmetry fail to explode via the delayed neutrino-heating mechanism (A. Mezzacappa et al. 2001; M. Rampp & H. T. Janka 2002; T. A. Thompson et al. 2003; M. Liebendörfer et al. 2004; K. Sumiyoshi et al. 2005). This poses a limitation for many open questions that rely on successful explosions, e.g., predicting supernova nucleosynthesis yields, unveiling the progenitor–remnant connection, and many more. One approach around this limitation is the use of so-called effective models. These are simulations in spherical symmetry where one aspect of multi-dimensional simulations is parameterized and the parameters are calibrated against observations. For example, P-HOTB (T. Ertl et al. 2016) uses a simple approximation of increased neutrino luminosities from the PNS. The PUSH method (A. Perego et al. 2015; K. Ebinger et al. 2019) instead parameterizes the effectively enhanced neutrino energy deposition in the gain layer that is seen in multidimensional simulations. And finally, STIR (S. M. Couch et al. 2020) parameterizes the strength of turbulence that is observed in multidimensional simulations in a mixing-length type parameterization. Welcomely, modern *multidimensional* simulations have achieved unaided explosions (H. T. Janka et al. 2007; H.-T. Janka 2017; S. M. Couch 2017; T. Kuroda et al. 2020; R. Bollig et al. 2021; K. Nakamura et al. 2022; D. Vartanyan et al. 2022; B. Sykes & B. Müller 2024; S. Shibagaki et al. 2024; T. Wang & A. Burrows 2024), demonstrating the viability of the delayed neutrino-heating mechanism and emphasizing the

importance of multidimensional effects in aiding explosions. One of these multidimensional effects is fluid turbulence.

As a result of the violent fluid motion in the gain region of the supernova, the low viscosity, and the significant shear stress, the fluid (or some fraction of it) can become turbulent due to instabilities. High-resolution studies of turbulence in 3D simulations of CCSNe (J. W. Murphy & C. Meakin 2011; R. Fernández 2012; J. C. Dolence et al. 2013; E. Endeve et al. 2013; T. Handy et al. 2014; E. Abdikamalov et al. 2015; S. M. Couch & C. D. Ott 2015; D. Radice et al. 2016; J. Casanova et al. 2020) are able to see the inertial range of the turbulence (D. Radice et al. 2016) and the "turbulence bottleneck"—the accumulation of power in the inertial scales of the turbulence (G. Falkovich 1994; W. Dobler et al. 2003; E. Abdikamalov et al. 2015; G. G. Katul et al. 2015). Turbulence has the potential to serve as an aid to the shock revival by stiffening the effective adiabatic index of the fluid. However, this conclusion about the effect of turbulence is inherently dependent on how the amount of turbulence present is measured, which is a notoriously difficult problem (A. Tsinober 2004).

The purpose of this paper is to investigate how different measures of turbulence in a CCSNe alter the conclusions one draws about its effect upon the explosion. To explore this question, we have undertaken four simulations of CCSNe spanning initial masses from $15M_\odot$ to $27M_\odot$. The simulations were performed in three spatial dimensions using the ELEPHANT code (M. Liebendörfer et al. 2009; R. Käppeli et al. 2011; R. M. Cabezón et al. 2018). This code is well suited to this study because of its good spatial resolution below the shock. We leverage this high resolution in the gain region to explore three different methods to compute turbulence. Using a variety of post-processing tests, we show that the three methods produce results that are not consistent with one another, in turn presenting the strengths and potential drawbacks of each method.

Our paper is organized as follows. The code we use, the progenitors, and general results of the simulations are described in Section 2. We next discuss in Section 3 the different methods we will use for measuring the turbulence, and then apply the measures to the simulations in Section 4. Finally, in Section 5, we examine how turbulence alters the effective adiabatic index of the fluid and how this index evolves with time in the simulations. We summarize and present our conclusions in Section 6.

2. The Simulations

2.1. The ELEPHANT Code

The ELEPHANT code solves the ideal hydrodynamics equations in a modified Newtonian gravitational potential together with the isotropic diffusion source approximation (IDSA) for the neutrino transport scheme. The code uses operator splitting between the solutions of the hydrodynamic equations and the neutrino transport equations. In the hydrodynamics module, which has roots in the FISH code described in R. Käppeli et al. (2011), the following conservation laws coupled with gravitational source terms are numerically solved in three spatial dimensions:

$$\frac{\partial \rho}{\partial t} + \boldsymbol{\nabla} \cdot (\rho \, \boldsymbol{v}) = 0, \qquad (1)$$

$$\frac{\partial}{\partial t}(\rho \, v_i) + \frac{\partial}{\partial x_j}(\rho \, v_i \, v_j + P_{\text{thermal}} \, \delta_{ij}) = -\rho \, \frac{\partial \phi}{\partial x_i}, \qquad (2)$$

$$\frac{\partial E}{\partial t} + \boldsymbol{\nabla} \cdot [(E + P_{\text{thermal}}) \, \boldsymbol{v}] = -\rho \, \boldsymbol{v} \cdot \boldsymbol{\nabla}\phi, \qquad (3)$$

$$\frac{\partial}{\partial t}(\rho \, Y_e) + \boldsymbol{\nabla} \cdot (\rho \, Y_e \, \boldsymbol{v}) = 0, \qquad (4)$$

$$\frac{\partial}{\partial t}(\rho \, Y_\nu^t) + \boldsymbol{\nabla} \cdot (\rho \, Y_\nu^t \, \boldsymbol{v}) = 0, \qquad (5)$$

$$\frac{\partial}{\partial t}\left[(\rho \, Z_\nu^t)^{\frac{3}{4}}\right] + \boldsymbol{\nabla} \cdot \left[(\rho \, Z_\nu^t)^{\frac{3}{4}}\boldsymbol{v}\right] = 0, \qquad (6)$$

$$\boldsymbol{\nabla}^2 \phi = 4 \, \pi \, G \, \rho, \qquad (7)$$

where the calculated unknowns with respect to space x_i and time t are the baryonic mass density ρ, velocity v_i, electron fraction Y_e, and the gravitational potential ϕ. While ELEPHANT is able to include magnetic fields, the magnetic field terms have been set to zero for this study. The temperature T is not explicitly seen in these equations, it is represented in the specific internal energy $e = e(\rho, T, Y_e)$, and the total energy $E = \rho \, e + \rho \, v^2/2$. As usual, G is the gravitational constant. We compute the thermal pressure $P_{\text{thermal}} = P_{\text{thermal}}(\rho, T, Y_e)$ using the LS220 equation of state (EOS) with an incompressibility parameter $K = 220$ MeV (J. M. Lattimer & F. D. Swesty 1991). Equations (5) and (6) advect the trapped neutrino fractions, Y_ν^t, and a multiple of the neutrino entropies, $(\rho Z_\nu^t)^{3/4}$ (where Z_ν is the mean neutrino specific energy) from the neutrino transport. The gravitational potential is modified following A. Marek et al. (2006) to include general relativistic corrections to the Newtonian potential.

The hydrodynamics Equations (1)–(7) are solved using the second-order relaxation scheme of S. Jin & Z. Xin (1995). To enforce that the scheme is total variation diminishing (a nonlinear constraint to ensure stability), ELEPHANT implements the minmod limiter in supersonic flow regimes and the van Leer limiter in subsonic regimes (R. Käppeli et al. 2011). For the time integration, a second-order predictor–corrector method is used.

For the neutrino transport, the ELEPHANT code uses the IDSA (M. Liebendörfer et al. 2009). The underlying idea of IDSA is that the neutrinos are separated into a trapped neutrino distribution function, f_ν^t, and a free-streaming neutrino distribution function, f_ν^s. These two components are then evolved separately. The trapped neutrino distribution functions are constructed from Y_ν^t and Z_ν^t assuming a thermal spectrum. Then, the diffusion equation, given as

$$\frac{1}{c}\frac{\partial f_\nu^t}{\partial t} = j_\nu - (j_\nu + \chi_\nu)f_\nu^t - \Sigma_\nu, \qquad (8)$$

where

$$\Sigma_\nu = \min\left\{\max\left[\alpha_\nu + \frac{1}{2}(j_\nu + \chi_\nu)\int f_o^s \, d\mu, \, 0\right], j_\nu\right\}, \qquad (9)$$

with

$$\alpha_\nu = \boldsymbol{\nabla} \cdot \left(\frac{-1}{3(j_\nu + \chi_\nu + \phi_\nu)}\boldsymbol{\nabla}f_\nu^t\right), \qquad (10)$$

is solved in three dimensions. In these equations, f_o^s denotes the use of the streaming neutrinos from the previous time step, j_ν is the spectral neutrino emissivity, χ_ν is the neutrino absorptivity, and ϕ_ν includes isoenergetic scattering in the mean free path (see S. W. Bruenn 1985). The nonlocal value α_ν, a descriptor of the evolution of trapped neutrinos, is computed by explicit finite differencing, with all other unknowns solved locally using an implicit Euler time step in which the solution is found using the Newton–Raphson iterative solver. The numerical solution of Equation (8) sets the net interaction rates between the matter and neutrino radiation and updates the electron fraction Y_e and the specific internal energy e so that they are consistent. The rates j_ν, χ_ν, and ϕ_ν are then used to update the trapped neutrino fraction Y_ν^t and mean energy Z_ν^t seen in Equations (5) and (6). This iterative method is easily parallelizable for IDSA because the only nonlocal value α_ν is computed explicitly, thus implying that zones do not need to communicate with each other within the iterative solve.

ELEPHANT uses a unique combination of 3D and 1D grids as its computational domain. The innermost computational domain consists of a 3D Cartesian cuboid. The 1D domain extends from the center of the supernova out well beyond the 3D domain, and thus well into the outer layers of the progenitor star. The inner 3D grid uses a uniform fixed grid spacing, while the larger, spherically symmetric 1D domain surrounding the 3D cuboid is evolved on an adaptive grid using the Agile-IDSA solver (M. Liebendörfer et al. 2009). More details of how the hydro and neutrino transport equations are solved on the 3D uniform Cartesian mesh, together with test cases, can be found in R. Käppeli et al. (2011). The spherically symmetric solution of the hydro and neutrino transport equations on the 1D grid is used primarily for the properties of the material falling through the boundary of the 3D mesh, but since it extends into the inner part of the Cartesian grid, it also provides a second solution of the equations that is especially useful within the PNS where it serves as a check of the entropy evolution. In addition, the combination of the two grids with the 1D solution extending well beyond the 3D gives ELEPHANT the ability to enlarge the 3D Cartesian cuboid if necessary. With this setup of the computational domain, the ELEPHANT code has high 3D spatial fidelity in the region below the shock, without the burden of a large number of grid zones where the solution is spherically symmetric. Hence, it is ideally suited for the proposed study of the post-bounce phase, especially for the growth of the turbulence in the shocked material. For each simulation in this study, we adopt a uniform fidelity of 1 km throughout the 3D volume; initially, the 3D volume encompasses the innermost 600 km of the star (i.e., along each axis, the 3D Cartesian coordinate ranges from -300 to $+300$ km). A direct comparison of the resolution of the 3D volume with the resolution of the grids adopted elsewhere in the literature for studies of turbulence in supernovae is challenging because of the wide variety of methods used: see, for example, the grids used in the studies by H. Nagakura et al. (2019) and J. Casanova et al. (2020). The most similar studies to this work are those of E. Endeve et al. (2012, 2013), which were also Cartesian and where the highest-resolution simulation used a cell spacing of 1.17 km.

2.2. General Properties of the Simulations

For this study, we consider four solar-metallicity progenitor stars of 15, 20, 23, and 27 $M_\odot$ zero-age main sequence (ZAMS) mass (S. E. Woosley & A. Heger 2007). Throughout this paper we shall refer to each simulation by reference to the progenitor model using the code "sXX" where XX is the ZAMS mass in units of the solar mass. Two of these progenitors (s15 and s20) have been extensively used in the literature. For the s20 model, explosions (S. W. Bruenn et al. 2016; A. Summa et al. 2016) and nonexplosions (M. A. Skinner et al. 2016; D. Vartanyan et al. 2018) were obtained in 2D simulations. Similarly, successful and failed explosions are also reported from 3D simulations of s20, depending on the exact simulation setup and on the physics included (e.g., T. Melson et al. 2015a; C. D. Ott et al. 2018; R. Glas et al. 2019; T. Kuroda et al. 2020). The s20 model seems to be close to the threshold between successful and failed explosions, warranting further investigations. For the s15 model, the picture is slightly more consistent, in the sense that most simulations find successful explosion, albeit as late as $\sim$400–500 ms post-bounce (however, see, e.g., Y. Suwa et al. 2016 for a failed explosion in 2D). The s23 model was chosen because it is a model that often fails to explode in effective 1D simulations using the STIR or PUSH method. In a recent 3D simulation of a different 23 $M_\odot$ model, the shock evolution follows other nonexploding models for the first $\sim$300 ms post-bounce, then hovers around 170 km for another $\sim$300 ms, and finally expands to 500 km only at 700 ms post-bounce (D. Vartanyan et al. 2023). Finally, the s27 model has been used in 3D simulations, where it exhibited a shock evolution similar to that of the s20, with shock runaway occurring at $\sim$200 ms (C. D. Ott et al. 2018). For an earlier version of the s27 (from S. E. Woosley et al. 2002), no shock revival was found in 3D simulations (F. Hanke et al. 2013; T. Takiwaki et al. 2021).

As stated previously, the simultaneously computed spherically symmetric solution on the 1D grid allows ELEPHANT to expand the 3D domain if necessary. We used this feature of the code to expand the 3D domain when the maximum shock radius in the 3D solution approaches the edge of the 3D computational domain. At this point, we expand the 3D domain by adding 100 grid zones in both the negative and positive directions along each coordinate axis. The new zones have the same 1 km resolution, and the 1D solution is used to fill the fluid and neutrino variables of the new zones. We undertook this 3D domain expansion twice during the s15, s20, and s27 simulations and stopped when any Cartesian coordinate of the maximum shock position reached 500 km. This technique of expanding the 3D volume as the shock approaches the edge was also used by E. Endeve et al. (2012).

In Figure 1, we show the average shock radius (various line styles) for each simulation along with its minimum and maximum position (shaded bands). During the first $t_{pb} \approx$ 70 ms, the shock evolves similarly with post-bounce time t_{pb} for all simulations. In each simulation, the shock forms and propagates outward to 140 km, at which point it stalls. After $t_{pb} \gtrsim 70$ ms, differences in the shock evolution between the four simulations start to emerge. The s15 simulation has the earliest shock revival (at $\sim$80 ms post-bounce), only $\sim$10 ms after the shock front starts to deform, which can be seen in the figure as the increasing spread between the minimum and maximum shock radius. The s20 and s27 simulations behave similarly,
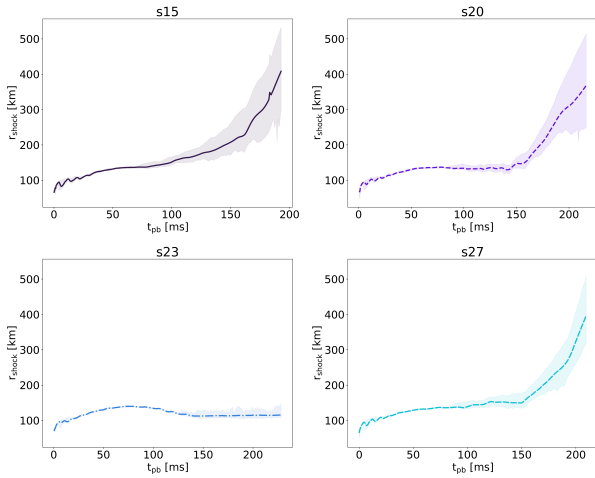
Figure 1. Average shock radii (lines), together with the minimum and maximum shock radii (shaded bands) as a function of the post-bounce time for all four simulations. The simulations end when the shock radius reaches the boundary of the largest (500 km) 3D domain. Note that the s23 simulation does not undergo a successful shock revival during the simulation time.

albeit with shock revival and the emergence of asphericity occurring later than in the s15 simulation. Moreover, there is a longer delay of ∼60 ms between when the shock starts to deviate from spherical symmetry and the clear shock expansion for the s20 and s27 simulations. At the end of our s15, s20, and s27 simulations, the shock appears to be irrevocably expanding outward. Following the common definition for successful explosions found in the literature (when the shock reaches 500 km), these models could be called successfully exploding, even though it is too early for the total energy in the gain region and above to have reached positive energies by $t_{pb} \sim 200$ ms. Finally, the s23 simulation does not show shock revival during the simulation time (∼205 ms post-bounce). Instead, the shock radius hovers around 100 km until the end of the simulation. This is qualitatively similar to the initial shock evolution of a different $23\,M_\odot$ model (from T. Sukhbold et al. 2018), which follows the nonexploding models for the first 300 ms, then continues to hover around 150 km, and only starts expanding around 600 ms post-bounce.

Figure 2 presents snapshots of the fluid entropy per baryon for all four simulations. In each snapshot, we observe low-entropy material ahead of the shock, as well as in the center of the computational domain, where the PNS is forming. The higher-entropy region in between contains the gain layer, which we define as the region interior to the shock where the entropy exceeds $5\,k_B$/baryon, the density is less than $\rho < 10^{10}\ \mathrm{g\,cm^{-3}}$, and the energy gained from electron neutrino and antineutrino absorption exceeds the energy lost by neutrino emission. We will focus our attention on this gain region in the next sections, and going forward, we have truncated our time-series data to begin when we have qualitatively determined a meaningful gain region has formed (at $t_{pb} \approx 61$ ms).

In Figure 2, we demonstrate the evolution of the supernovae using selected snapshots from each simulation. The first three columns correspond to $t_{pb} = 100, 150, 195$ ms post-bounce, and the last column represents the final simulation time for each simulation. In the case of s15, the shock reached 500 km before 195 ms post-bounce, and thus the final panel is left blank. In the s15, s20, and s27 simulations, the spherical

symmetry of the simulation is visibly broken when neutrino heating initiates convection in the gain region. By 150 ms post-bounce, the shocks in these three simulations are noticeably aspherical. By ∼195 ms post-bounce, low-entropy downflows through the gain layer amid large convective plumes are clearly visible.

For the s23 simulation, the spherical symmetry remains largely preserved for the entire duration of the simulation. Although some of the materials in the gain region reach specific total energies comparable to those in the other three simulations, the energy gained by neutrino absorption is clearly not enough to revive the shock in this case. The reader may notice that the center of the quasi-circular shock front is slightly displaced from the origin of the coordinates. Indeed, from animations of the entropy as a function of post-bounce time, we observed an oscillatory motion of the shock starting at $t_{pb} \sim 150$ ms characteristic of a SASI (J. M. Blondin et al. 2003; J. M. Blondin & A. Mezzacappa 2007). This timescale is similar to the timescale of a spiral SASI in a magnetized $24\,M_\odot$ model by K. Nakamura et al. (2025).

We can be more quantitative about the time at which convection begins in each simulation by computing the fraction of kinetic energy within the gain layer that is in the nonradial directions:

$$E_{\mathrm{transverse}}/E_{\mathrm{kin}}$$
$$= \int_{V_{\mathrm{gain}}} \rho \left(v_\theta^2 + v_\phi^2 \right) dV \Big/ \int_{V_{\mathrm{gain}}} \rho \left(v_r^2 + v_\theta^2 + v_\phi^2 \right) dV, \quad (11)$$

where v_r, v_θ, v_ϕ are the radial, polar, and azimuthal components of the velocity and V_{gain} is the volume of the gain region, defined above. This ratio is shown in Figure 3. For the s15, s20, and s27 simulations, the fraction of the kinetic energy in the transverse (i.e., nonradial) directions rises very rapidly between $t_{pb} \sim 60$ ms and $t_{pb} \sim 100$ ms as the shock stalls. The rise is earlier in the s15 simulation than in the s20 and s27 simulation, but by $t_{pb} \sim 100$ ms they all reach the level of 30%–40%, with a slow growth of the ratio thereafter. Interestingly, the figure shows that the fraction of kinetic energy in the transverse directions begins to grow in the s23 simulation, starting at $t_{pb} \sim 120$ ms. Even though the s23 simulation is not exploding—the shock is not seen to be advancing in Figure 1 and we shall shortly show more evidence that further indicates this conclusion—the high densities and large angular motions present in this simulation due to the SASI mean that the ratio of the transverse and total kinetic energy in the gain region becomes comparable to the same ratio of energies in the successful explosions. While it does not reach the ∼40% level seen in the other three simulations, it is only smaller by a factor of ∼2 at $t_{pb} = 200$ ms.

We want to turn our analysis to the mechanism by which the shock is revived in our simulations. In a neutrino-driven explosion, the shock is revived due to neutrino-heated material in the gain region being brought up to the shock by convection and buoyancy. Shock revival occurs when the material within the gain region has sufficient time to absorb enough of this heating energy to overcome gravity. Thus, the revival time can be estimated by comparing the heating timescale to the advection timescale through the gain region. For the advection timescale, we adopt the definition used in
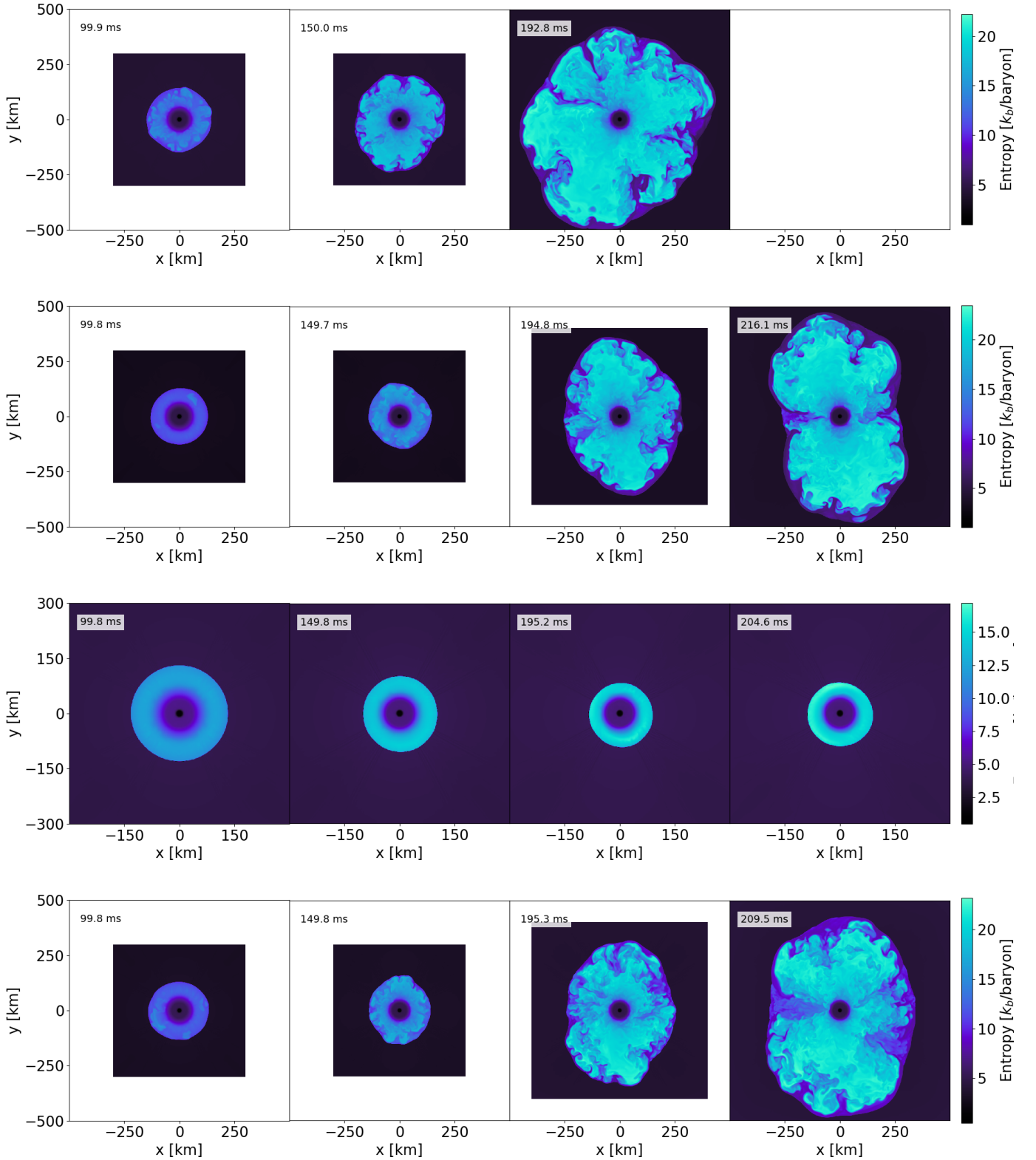
Figure 2. Entropy maps in the *xy*-plane for the s15 (top), s20 (second row), s23 (third row), and s27 (bottom row) simulations at ∼100 ms (first column), ∼150 ms (second column), ∼195 ms (third column) post-bounce, and at the final simulation time (last column). Note the smaller spatial scale and entropy scale for s23.

R. Buras et al. (2006):

$$\tau^*_{\mathrm{adv}}(t_1) = t_2(M) - t_1(M), \tag{12}$$

where $t_2(M)$ is the time at which a mass M is enclosed by the shock and $t_1(M)$ is the time at which that same mass falls beneath our gain region. The neutrino-heating timescale is
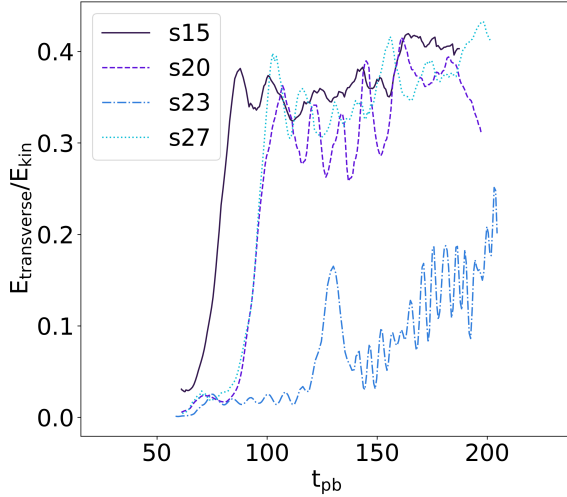
Figure 3. Ratio of the transverse energy to the total kinetic energy in the gain region as a function of the post-bounce time for the s15 (solid), s20 (dashed), s23 (dotted–dashed), and s27 (dotted) simulations.

defined as the amount of time that material in the gain region would need to be exposed to the current neutrino-heating rate to become gravitationally unbound, i.e.,

$$\tau_{\text{heat}} = \frac{|E_{\text{gain}}|}{\dot{Q}_{\text{heat}}}, \qquad (13)$$

where $E_{\text{gain}} = E_{\text{kin}} + E_{\text{int}} + E_{\text{grav}}$ is the total energy in the gain region, E_{int} and E_{grav} are, respectively, the total internal and total gravitational energy of the fluid in the gain region, and $\dot{Q}_{\text{heat}}$ is the total neutrino-heating rate in the gain region. It is found that, when the ratio of the advection timescale to the heating timescale, $\tau_{\text{adv}}/\tau_{\text{heat}}$, exceeds unity, the stalled shock is considered revived, and on average, the shock begins to move outward due to the increased energy of the enclosed material (H. T. Janka & W. Keil 1998; H. T. Janka 2001; T. A. Thompson et al. 2005; J. W. Murphy & A. Burrows 2008). Note that this does not guarantee an explosion, but simply is an indicator of an outward-moving shock. Figure 4 shows the ratio of these two timescales for all four simulations, with the line for a ratio of unity highlighted in gray. From Figure 4, we see that this ratio exceeds unity in the s15, s20, and s27 simulations at times that closely match the shock revival times seen in Figure 1, supporting a neutrino-driven explosion mechanism for these simulations. For the s23 simulation, the ratio never exceeds unity, which is consistent with the lack of a shock revival in this simulation.

Another diagnostic invoked to investigate the phase leading up to shock revival consists of examining the mass inflow rate through the shock front ($\dot{M}_{\text{shock}}$) and the mass inflow rate onto the PNS ($\dot{M}_{\text{PNS}}$). The comparison of these rates are shown in Figure 5. Initially, $\dot{M}_{\text{shock}}$ and $\dot{M}_{\text{PNS}}$ are firmly related. In the first few tenths of milliseconds post-bounce, $\dot{M}_{\text{shock}}$ decreases more rapidly than $\dot{M}_{\text{PNS}}$ and the initial shock turns into a standing accretion shock. Once nonradial fluid motion starts to develop around 60–100 ms post-bounce, we observe a drop in $\dot{M}_{\text{PNS}}$ (while $\dot{M}_{\text{shock}}$ continues to decrease smoothly), resulting in the increase of $\dot{M}_{\text{shock}} - \dot{M}_{\text{PNS}}$. Once the stalled shock starts expanding again, $\dot{M}_{\text{PNS}}$ is smaller than $\dot{M}_{\text{shock}}$ and $\dot{M}_{\text{shock}} - \dot{M}_{\text{PNS}}$ reaches zero or slightly positive values. While the difference $\dot{M}_{\text{shock}} - \dot{M}_{\text{PNS}}$ is similar for all four simulations, the individual
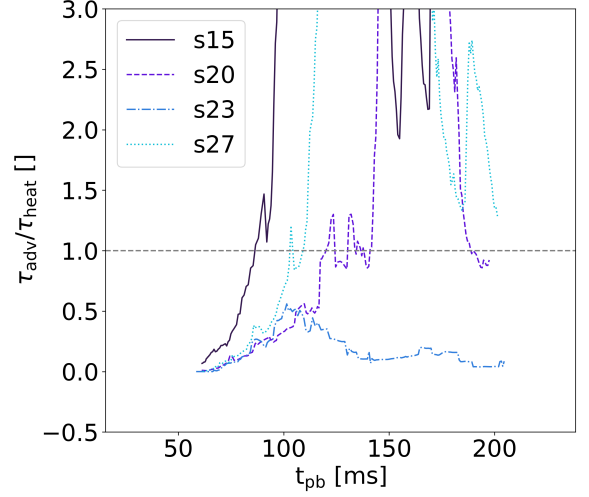
Figure 4. The ratio of advection timescale to heating timescale as a function of the post-bounce time for all four simulations. The gray dotted line marks where the ratio equals unity.
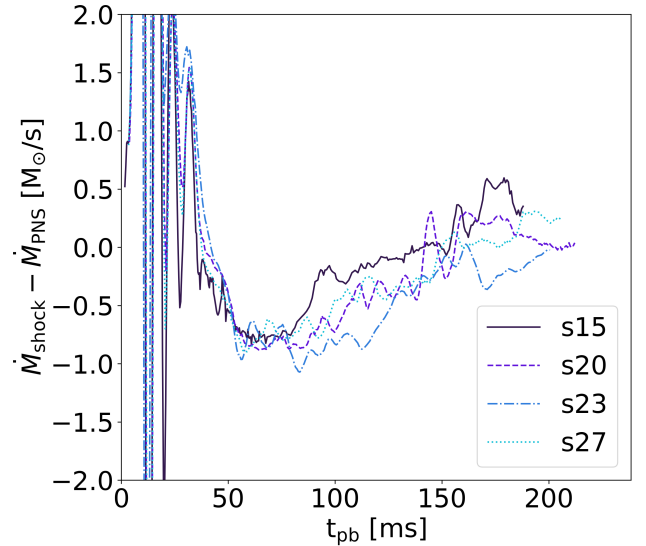
Figure 5. Difference between the mass accretion rate through the shock front ($\dot{M}_{\text{shock}}$) and the mass accretion rate onto the PNS ($\dot{M}_{\text{PNS}}$) as a function of the post-bounce time for all four simulations. The data are smoothed over a 5 ms window.

amount of accretion through the shock ($\dot{M}_{\text{shock}} - \dot{M}$) and onto the PNS ($\dot{M}_{\text{PNS}}$) are higher for the s23 model (no shock expansion) than for any of the other models (with shock expansion), by up to a factor of 2 after ~90 ms after bounce

In summary, the results from our simulations shown in Figures 1 through 5 are broadly consistent with other 3D simulations (S. M. Couch & C. D. Ott 2013; S. M. Couch & E. P. O'Connor 2014; I. Tamborra et al. 2014; A. Mezzacappa et al. 2015; H. Andresen et al. 2017; D. Vartanyan et al. 2018; R. Glas et al. 2019; B. Müller & V. Varma 2020; D. Vartanyan et al. 2023; J. Powell & B. Müller 2024; S. Shibagaki et al. 2024; S. Shankar et al. 2025).

3. Measuring the Turbulence

The turbulence in the gain region is conjectured to be an important ingredient in revival of the shock (S. M. Couch &

C. D. Ott 2015). The prevailing theory is that the average adiabatic index of the turbulence (which we shall define later in Section 5) is larger than in a nonturbulent fluid (S. M. Couch & C. D. Ott 2015; T. Melson et al. 2015b; D. Radice et al. 2018; A. Burrows & D. Vartanyan 2021; J. Matsumoto et al. 2024). To investigate how the turbulence affects the simulations, it is first necessary to define a measure of the amount of turbulence. This is not a straightforward task; as discussed in R. J. Adrian et al. (2000), there is no one, perfect measure of turbulence.

In some previous studies of turbulence in supernovae (F. Hanke et al. 2012; J. C. Dolence et al. 2013; S. M. Couch & E. P. O'Connor 2014; R. Fernández et al. 2014), the reader will find the turbulent kinetic energy E_{turb} defined to be equivalent to the nonradial kinetic energy, i.e.,

$$E_{\mathrm{turb}} \equiv E_{\mathrm{transverse}} = \int_{V_{\mathrm{gain}}} \frac{\rho}{2} \left(v_\theta^2 + v_\phi^2 \right) dV. \qquad (14)$$

This definition of the turbulent kinetic energy obviously does not include any contribution from flow in the radial direction that could be turbulent, but it does include a contribution from the nonradial flow that may not be turbulent; e.g., flows that are simply the lateral motion of the fluid at the top of convective plumes and/or any global rotational motion of the fluid due to a SASI. We shall not consider this definition further in this paper.

Another commonly encountered approach for measuring the amount of energy stored in turbulence is to invoke a Reynolds decomposition of the velocity field and then define the turbulent kinetic energy as

$$E_{\mathrm{turb}} = \int_{V_{\mathrm{gain}}} \frac{\rho}{2} \left| \boldsymbol{v} - \langle \boldsymbol{v} \rangle \right|^2 dV, \qquad (15)$$

where $\langle \boldsymbol{v} \rangle$ is an expectation value for the velocity. Note that $\langle \boldsymbol{v} \rangle$ can be a function of position and time. Defining the expectation value is not straightforward; in statistically steady-state flows, the expectation value for the velocity $\langle \boldsymbol{v} \rangle$ is the time-averaged velocity of the fluid at a given location. While it is certainly possible to time-average fluid properties in a supernova simulation, it is conceptually difficult to accept them as useful, because the system is not close to a statistical steady state (even during the period when the shock has stalled). Instead, authors usually substitute a spatial average of the the fluid velocity in place of a time average at a given location. However, spatial averages are just as conceptually fraught in situations where the fluid may have organized large-scale motions, i.e., on scales close to the dimensions of the fluid volume. In the case of a supernova, these large-scale motions are due to convection and/or SASI. Since there is no clear way to define $\langle \boldsymbol{v} \rangle$, we have considered two different spatial average options.

The first method we adopt, we denote as the spherical spatial average (SSA); it is based on S. M. Couch & C. D. Ott (2015). The SSA algorithm for computing $\langle \boldsymbol{v} \rangle$ is based on the observation that the general flow of the fluid in the gain region is toward the PNS. Thus, we define $\langle \boldsymbol{v} \rangle$ as $\langle v_r \rangle \, \hat{\boldsymbol{r}}$, where $\langle v_r \rangle$ is the average radial velocity for all zones at a given radius r. Since we do not use a spherical coordinate grid in our simulations, we implement this definition by finding all the Cartesian grid cells with a cell-center radius in a given 1 km

thick shell. Thus, we define

$$\langle v_r \rangle = \frac{1}{M_{\mathrm{shell}}} \int_{V_{\mathrm{shell}}} \rho \, v_r \, dV, \qquad (16)$$

with

$$M_{\mathrm{shell}} = \int_{V_{\mathrm{shell}}} \rho \, dV. \qquad (17)$$

Note that, when the shock becomes aspherical, only grid cells in the gain region are used to compute the average radial velocity; thus, the shell no longer forms a complete spherical surface.

The second method we consider, we call the local spatial average (LSA) method. In this method, we define the expectation value of the velocity, $\langle \boldsymbol{v} \rangle$, for a particular grid cell as being the mass-weighted average of the velocity in a cube surrounding the cell:

$$\langle \boldsymbol{v} \rangle = \frac{1}{M_{\mathrm{cube}}} \int_{V_{\mathrm{cube}}} \rho \, \boldsymbol{v} \, dV, \qquad (18)$$

where

$$M_{\mathrm{cube}} = \int_{V_{\mathrm{cube}}} \rho \, dV \qquad (19)$$

and V_{cube} is a cubic volume of side length L centered on the grid cell under consideration. Note that, when we perform the integral, the volume V_{cube} only includes those cells that are found to be in the gain region, implying that the volume is not always a complete cube. The size of the averaging volume must be chosen appropriately. In the limit where the size of the averaging volume becomes small, $\langle \boldsymbol{v} \rangle$ approaches the velocity of the grid cell under consideration, in which case the deviation of the velocity from the expectation value approaches zero, i.e., $\left| \boldsymbol{v} - \langle \boldsymbol{v} \rangle \right| \to 0$, and therefore the turbulent kinetic energy also approaches zero in this limit. We must select a suitable length scale for which the turbulent kinetic energy is captured.

The turbulent kinetic energy in the gain region for a snapshot at $t_{\mathrm{pb}} \approx 150$ ms computed using the LSA method as a function of the averaging volume scale L is shown in the left panel of Figure 6. As described above, when the averaging volume is small, the turbulent kinetic energy approaches zero. As the averaging volume grows, we see a rise in the turbulent kinetic energy but we do not observe a plateau, implying there is no range of averaging volume sizes where the turbulent kinetic energy is independent of the size of the averaging volume. At $L \sim 20$ km, we find a maximum in the derivative of E_{turb}, seen as a peak in right panel of Figure 6. Although there is not a clear range over which the turbulent kinetic energy is independent of the length scale, for the purposes of defining the turbulent kinetic energy using the LSA method, we have adopted a cube length scale of 20 km. We shall later show that this averaging volume scale is larger than the characteristic vortex radius (see Section 4.2).

Finally, we adopt a definition of the turbulent kinetic energy that we refer to as the spectral method, based upon the approach found in E. Endeve et al. (2013). A variation of this method can be found in J. Casanova et al. (2020). The spectral method forgoes trying to define $\langle \boldsymbol{v} \rangle$ directly and instead removes the large-scale fluid motion by excluding the small wavenumbers from a Fourier transform and then integrating
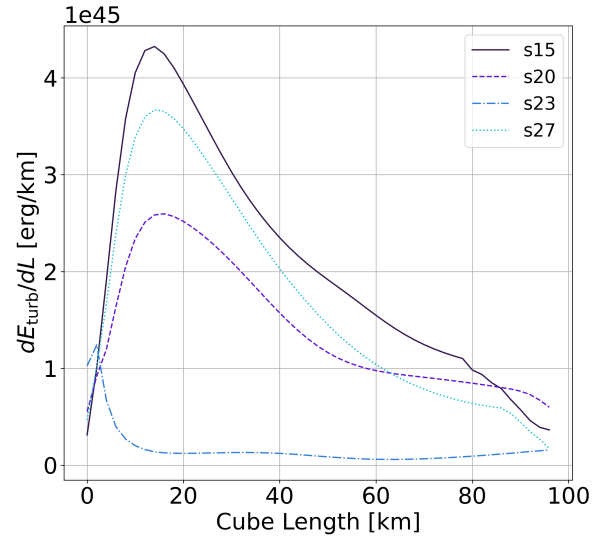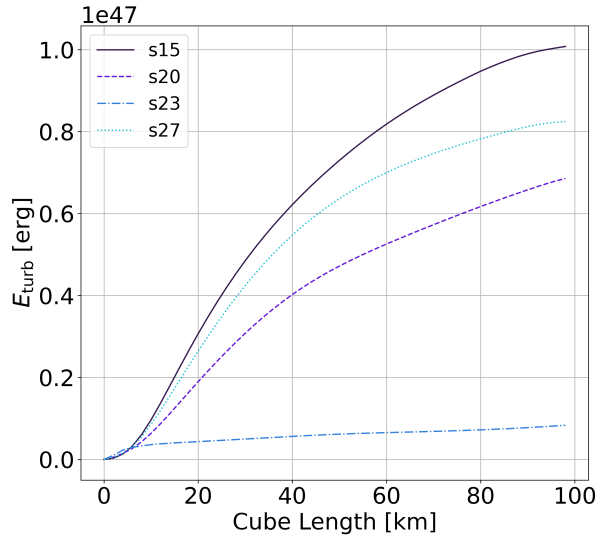
Figure 6. The total turbulent kinetic energy (left) and the corresponding slope of the total kinetic energy (right) as a function of the cube side length used in the LSA method at $t_{pb} \approx 150$ ms for all four simulations.

over the remaining range of wavenumbers. More precisely, let $\hat{\boldsymbol{f}}$ be the Fourier transform of an arbitrary vector quantity $\boldsymbol{f}$ in the gain region,

$$\hat{\boldsymbol{f}} = \frac{1}{(2\pi)^3} \int_{V_{gain}} \boldsymbol{f} \exp\left(2i\pi\, \boldsymbol{k} \cdot \boldsymbol{x}\right) d^3x. \quad (20)$$

Integrating the squared magnitude of the transformed quantity over a spherical shell in the k-space, one obtains the power spectrum,

$$\hat{e}_f(k) = \frac{1}{2} \int_{k\text{-shell}} |\hat{\boldsymbol{f}}|^2 k^2 \, d\Omega_k. \quad (21)$$

Adopting $\boldsymbol{f} = \sqrt{\rho}\, \boldsymbol{v}$ and including only data originating from the gain layer gives the power spectrum $\hat{e}_{\sqrt{\rho}\, \boldsymbol{v}}$ of the kinetic energy in the gain region. The *turbulent* kinetic energy is defined as the integral of the power spectrum above a minimum wavenumber, i.e.,

$$E_{turb} = \int_{k_{min}}^{\infty} \hat{e}_{\sqrt{\rho}\, \boldsymbol{v}} \, dk. \quad (22)$$

Here, k_{min} is the minimum wavenumber considered. As with the LSA method described above, we face the question of what to use for the minimum wavenumber k_{min}. E. Endeve et al. (2013) adopted $k_{min} = 0.1 \times (2\pi)$ km^{-1}; however, we have found that, for our simulations, this lower bound does not sufficiently capture the onset of convection, which was not present in E. Endeve et al. (2013). As such, we have followed their same method to determine a k_{min} suitable for our simulations.

If the fluid has well-developed turbulence, we expect the compensated spectral specific kinetic energy, defined to be $\hat{e}_v k^{5/3}$ where $\hat{e}_v$ is the spectrum of the specific kinetic energy, to be a constant for a range of wavenumbers k_r. We have plotted this compensated specific kinetic energy power spectrum in Figure 7 for all four simulations at $t_{pb} \approx 150$ ms. This figure can be compared with the left panel of Figure 3 in E. Endeve et al. (2013), although we caution the reader that (a) the definition of k in E. Endeve et al. (2013) means the wavenumbers there are 2π larger than those used in
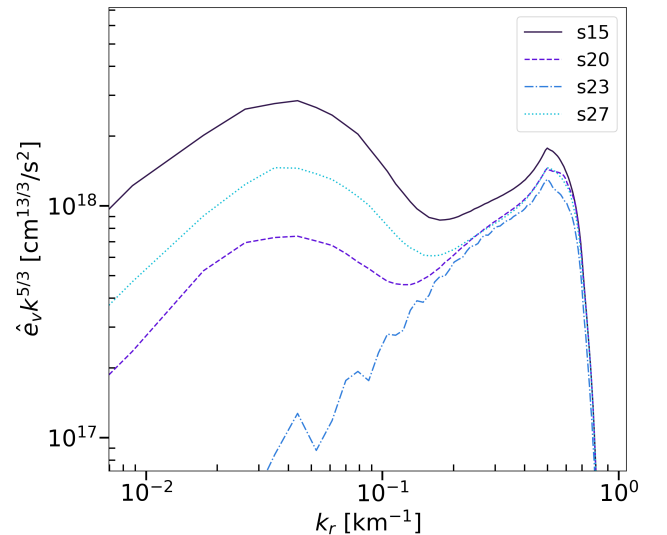

Figure 7. The compensated specific kinetic energy power spectrum at $t_{pb} = 150$ ms for all four simulations.

this paper, and (b) we show a range of wavenumbers shifted to slightly higher values. Examining Figure 7, we do not see a horizontal section—a region of wavenumbers where the compensated spectral specific kinetic energy is constant—in any of the curves in our plot, but in the three successful explosions we find a minimum in the spectrum at $k_r = 0.1$–0.2 km (corresponding to a physical scale of 5–10 km) and a maximum at $k_r \sim 0.04$; km (corresponding to a physical scale of 25 km). For the purposes of defining the turbulent kinetic energy using the spectral method, we set the lower bound of integration k_{min} to be $k_{min} = 0.025$ km^{-1}, equivalent to a physical scale of 40 km.

4. Application to Simulations

4.1. Turbulent Kinetic Energy

We compute the total turbulent kinetic energy in the gain region using the three methods described above. The results are shown in the top row of Figure 8. No matter the method used,
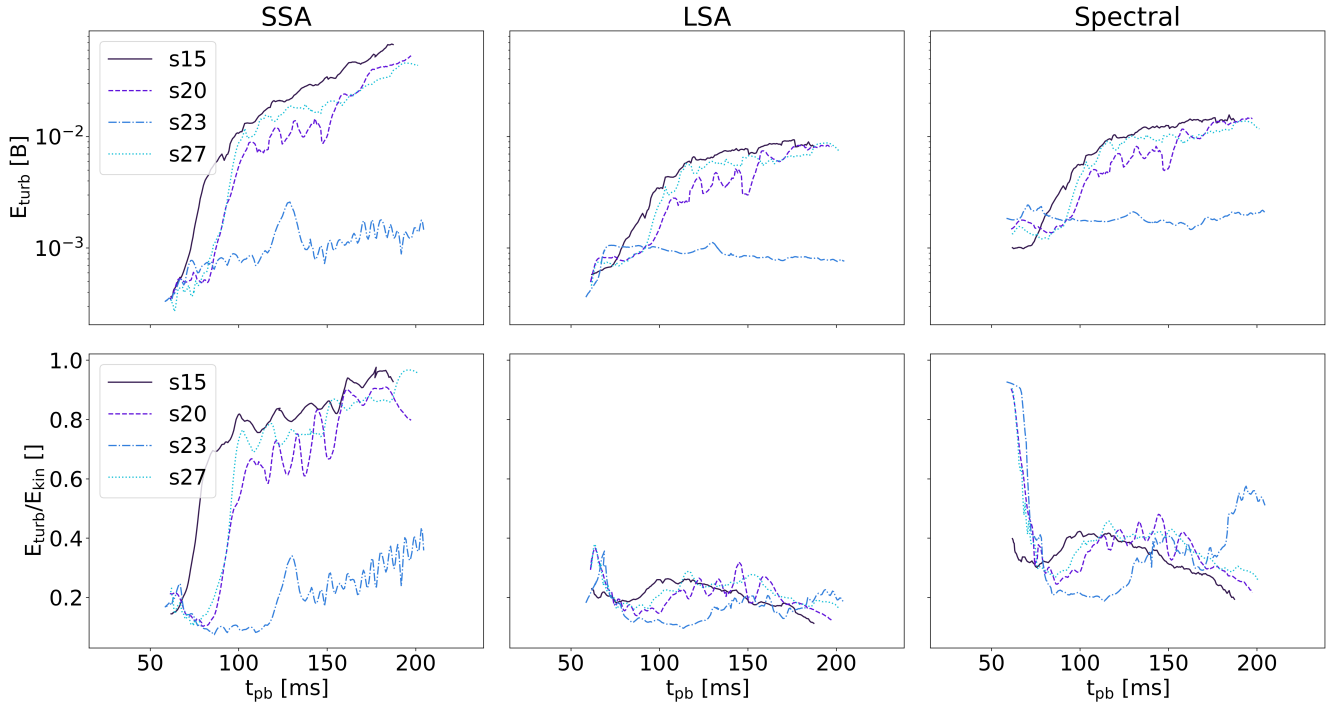
Figure 8. Top: the turbulent kinetic energy in the gain region as a function of the post-bounce time for all four simulations. Bottom: ratio of the total turbulent kinetic energy to the total kinetic energy in the gain region as a function of the post-bounce time for all four simulations. Each column represents a different method for computing the turbulent kinetic energy. Left: SSA method. Middle: LSA method. Right: spectral method.

for a successful explosion, there is a rapid increase in the amount of turbulent kinetic energy in the gain region when convection begins (80–100 ms post-bounce). Thereafter, the increase is more gradual in the interval $100 \text{ ms} \lesssim t_{\rm pb} \lesssim 200 \text{ ms}$. While the general trend of the results is the same across all methods, we note that the LSA and spectral methods give values consistently smaller than the SSA method, with the consequence that the growth in the turbulent kinetic energy during the interval $100 \text{ ms} \lesssim t_{\rm pb} \lesssim 200 \text{ ms}$ using the LSA and spectral methods is only by a factor ~ 2 compared to a factor closer to ~ 8 over the same period when using the SSA method.

The s23 simulation is clearly distinct from the successful explosions across all three methods. The amount of turbulent kinetic energy is smaller for s23 by approximately an order of magnitude (or more) compared to s15, s20, and s27. Moreover, there is little (if any) growth of the turbulent kinetic energy over the period $100 \text{ ms} \lesssim t_{\rm pb} \lesssim 200 \text{ ms}$ for the s23 simulation.

The difference between the amount of turbulent kinetic energy computed in the s23 simulation compared to the s15, s20, and s27 simulations is largely due to the difference in size/mass in the gain regions of the simulations. To eliminate this dependence, we show, in the bottom row of Figure 8, the evolution of the ratio of the turbulent kinetic energy to the total kinetic energy within the gain region, using each of the three methods. These panels reveal there are fundamental differences between the methods already hinted at by the previously noted differences in the growth rates of the turbulent kinetic energy in the top panels. Using the SSA method, there is still a clear distinction between a successful and a failing supernova in the energy ratio, but this distinction disappears in the ratios computed using the LSA and spectral methods. Note that the ratio of turbulent kinetic energy to total kinetic energy using the SSA method has a strong resemblance to Figure 3. When the SSA method is used, the ratio of turbulent kinetic energy to

total kinetic energy is on the order of $\sim 60\%$ in successful explosions at the onset of the explosion, and later rises to $\sim 80\%$ by the end of the simulation. The s23 stands apart from the other runs. Although the ratio of kinetic energies in s23 using the SSA method does not reach the same level as the successful explosions, there is still an overall growth of the ratio after $t_{\rm pb} \sim 120 \text{ ms}$ to $\sim 40\%$ by the end of the simulation. In contrast, the ratios of turbulent to total kinetic energy computed using the LSA or spectral method are very similar for all *four* simulations. There is no substantial distinction between successful and failing simulations. Aside from some temporary fluctuations, the ratio of energies lies between $\sim 20\%$ and $\sim 40\%$ for all four simulations after $t_{\rm pb} \sim 80 \text{ ms}$, with no apparent change during shock revival of the s15, s20, and s27 simulations. One feature of note is that, at approximately 195 ms post-bounce, there is an uptick in the percentage of turbulent energy calculated by the spectral method for s23. We posit that this uptick is related to the SASI that occurs in the s23 at late times. As the large-scale angular motion of the shock increases, these SASI modes begin to be detected by the Fourier transform.

The different methods for computing the turbulent kinetic energy clearly do not capture the same physics, and the differences would lead to different conclusions about the relative importance of turbulence for successful explosions. To further probe this, we turn our attention to other fluid quantities that are also associated with turbulence. For this, we focus on the three simulations that have a substantial amount of turbulence in the gain region: the s15, s20, and s27 simulations.

4.2. Enstrophy Comparison

Fluid vorticity, $\boldsymbol{\omega} = \boldsymbol{\nabla} \times \boldsymbol{v}$, or alternatively enstrophy $\epsilon = |\boldsymbol{\omega}|^2/2$, is also regarded as an intrinsic aspect of turbulence
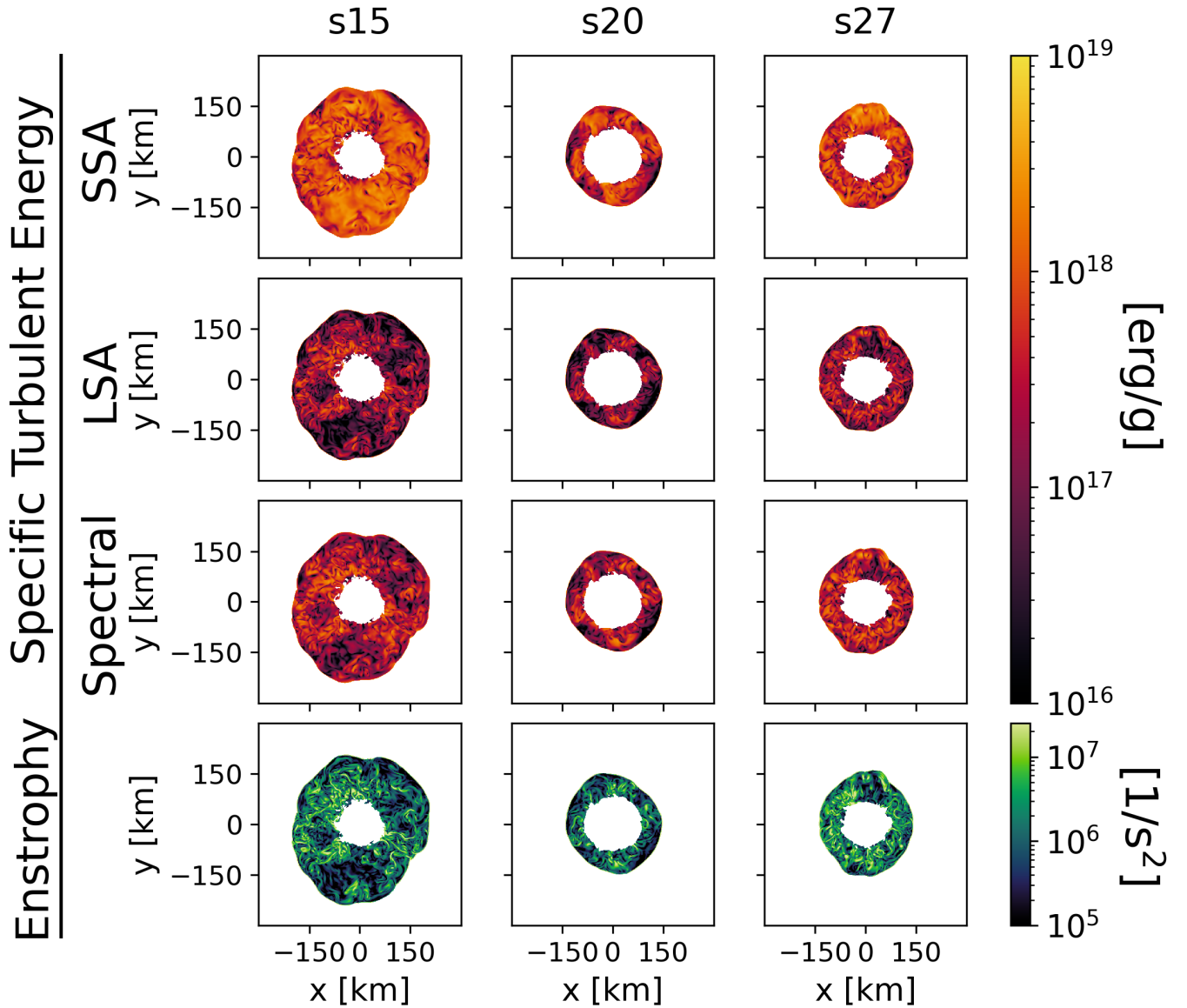
Figure 9. Spatial maps of the specific turbulent energy in the *xy*-plane computed using all three methods, for the exploding simulations. First row: SSA method. Second row: LSA method. Third row: spectral method. Bottom: Spatial maps of the enstrophy in the *xy*-plane for the same simulations. All panels are at 150 ms post-bounce.

(A. Tsinober 2004) and thus a good, but not sufficient, measure of its presence. Therefore, one might expect a map of the enstrophy should resemble a map of the specific turbulent kinetic energy e_{turb}. We present the spatial maps of the specific turbulent kinetic energy at the snapshot time of $t_{\text{pb}} = 150$ ms in Figure 9. These spatial plots are masked to show only the values in the gain region. For the spectral method, we generate the map by Fourier transforming the velocity $\boldsymbol{v}$, setting the amplitude of all Fourier modes to zero for all wavenumbers $k \leqslant k_{\text{min}}$, then transforming back to real space to produce the velocity field $\boldsymbol{u}$. Using $\boldsymbol{u}$, the specific turbulent kinetic energy for the spectral method is defined as $e_{\text{turb}} = |\boldsymbol{u}|^2/2$. Finally, the map of the enstrophy is also shown in the same figure in the bottom row for direct comparison.

Comparing these figures, we observe that, using either the LSA or spectral methods, the areas of greatest specific turbulent energy are coincident with the areas of greatest enstrophy. And similarly, areas where we find the lowest

amounts of specific turbulent kinetic energy are also areas with low enstrophy. In contrast, the SSA method yields maps where we observe regions with large amounts of specific turbulent kinetic energy but the enstrophy is low. These are regions where the fluid is moving outward, such as in convective plumes. At the other end of the scale, in places where the SSA finds only a small amount of specific turbulent kinetic energy, there is also a small amount of enstrophy. Thus, the amount of correlation between the maps of specific turbulent kinetic energy and enstrophy is larger when using the LSA or spectral methods than when using the SSA.

That the specific turbulent kinetic energy using the SSA is dominated by the convective plumes can be explained by examining how the expectation value for the velocity is defined for this method. In the SSA method, the average radial velocity $\langle v_r \rangle$ is computed from all the fluid on a spherical shell. Given that the general flow of the fluid in the gain region is toward the PNS, $\langle v_r \rangle$ will be negative. The specific turbulent
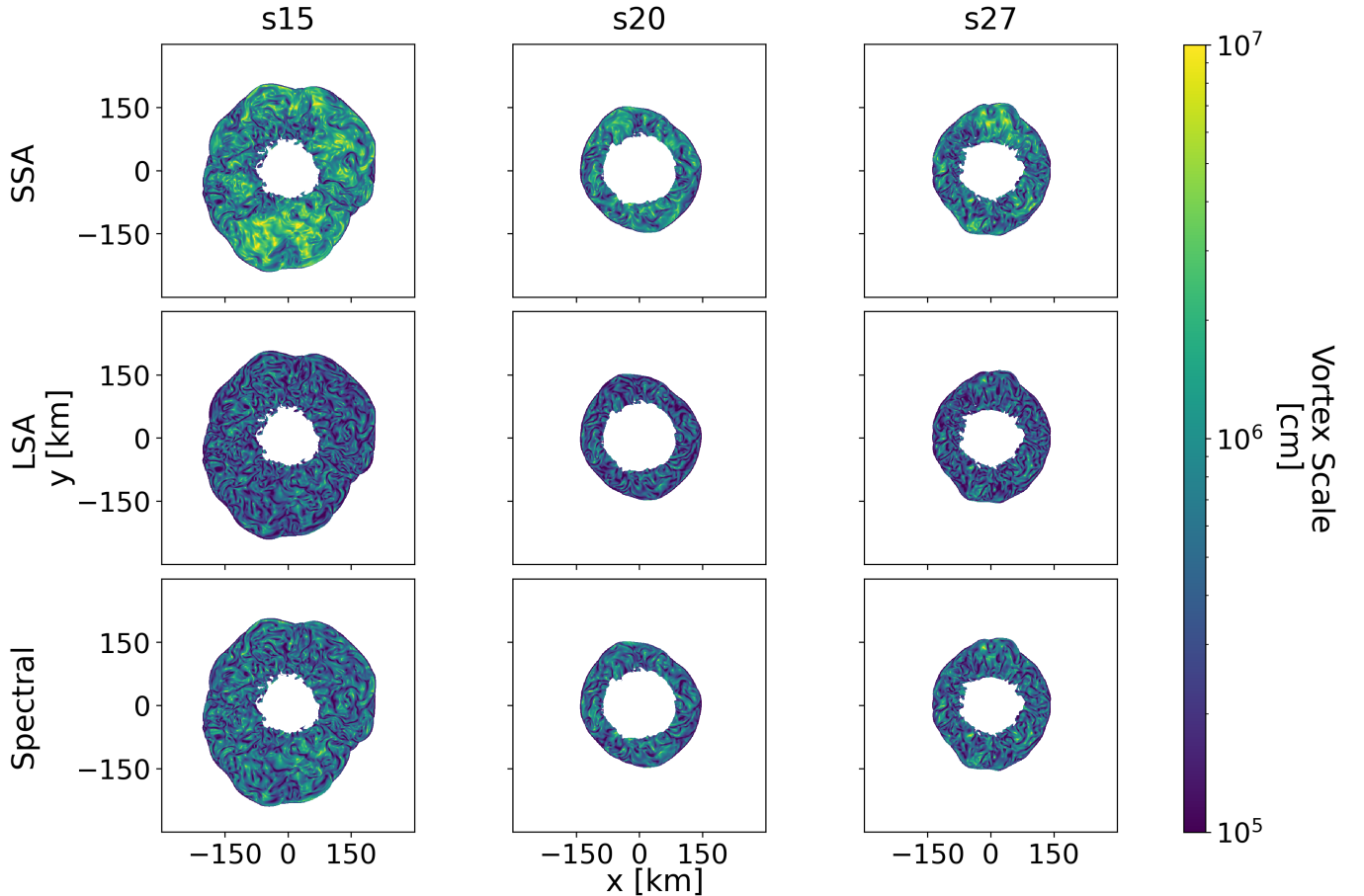
Figure 10. The vortex radius scale using the SSA (top row), LSA (middle row), and spectral methods (bottom row) for the s15, s20, and s27 simulations (from left to right). All panels are at 150 ms post-bounce.

kinetic energy for the SSA method is $e_{\mathrm{turb}} = |\boldsymbol{v} - \langle v_r \rangle \, \hat{\boldsymbol{r}}|^2/2$. For a fluid element that is moving outward, i.e., $\boldsymbol{v} \approx |\boldsymbol{v}|\,\hat{\boldsymbol{r}}$, the contribution to the specific turbulent kinetic energy is $e_{\mathrm{turb}} = (|\boldsymbol{v}| - \langle v_r \rangle \hat{\boldsymbol{r}})^2/2 \approx (|\boldsymbol{v}|^2 + \langle v_r \rangle^2 + 2\,|\boldsymbol{v}|\,|\langle v_r \rangle|)/2$. For a fluid element with an inward velocity, i.e., $\boldsymbol{v} \approx -|\boldsymbol{v}|\,\hat{\boldsymbol{r}}$, the contribution to the specific turbulent kinetic energy is approximately $e_{\mathrm{turb}} = (|\boldsymbol{v}|^2 + \langle v_r \rangle^2 - 2\,|\boldsymbol{v}|\,|\langle v_r \rangle|)/2$. Thus, outflows dominate the specific turbulent kinetic energy in the SSA method. In comparison, in the LSA method the expectation value for the velocity is computed from the local surrounding fluid. In a convective plume, the expectation value will point in approximately the same direction as the velocity of the fluid element under consideration, and so the deviation of the fluid velocity in the outflow will be smaller, thus leading to a much smaller contribution to the specific turbulent kinetic energy from a convective plume.

The calculation of the enstrophy also allows us to determine the characteristic scale for the turbulent vortices. Knowing this scale allows us to validate the choice of LSA averaging volume and the $k_{\min}$ chosen for the spectral method. We follow the method outlined in D. Ryu et al. (2000) and define the characteristic vortex scale as

$$\ell = \sqrt{e_{\mathrm{turb}}/\epsilon}, \tag{23}$$

where ϵ is the enstrophy. Note that D. Ryu et al. (2000) and E. Endeve et al. (2012) call this same quantity the "flow Taylor microscale." In Figure 10, we plot 2D slices of the characteristic

vortex scale using all the definitions of turbulence for the same snapshots as those shown in Figure 9. We find that the characteristic vortex scale using the LSA or spectral definitions of the turbulent kinetic energy is of a few kilometers over the entire gain region. This characteristic vortex scale is smaller than both the size of the averaging cube used ($L = 20$ km) in the LSA method and the $1/k_{\min}$ used in the spectral method ($1/k_{\min} = 40$ km). E. Endeve et al. (2012) use this same quantity to also justify their choice of $k_{\min}$. This is an indicator that the LSA and spectral methods are sufficiently capturing the turbulence. In contrast, using the SSA to compute the specific turbulent kinetic energy, we obtain a characteristic vortex scale that is generally larger than when using the LSA or spectral method. From Figure 10, we see that, when using the SSA method, the characteristic vortex scale can be as large as $\ell \sim 100$ km. A vortex of this size more closely resembles the size of the convective Bénard cells that extend across the gain region, rather than local turbulence.

In summary, we find that different definitions of the turbulent kinetic energy lead to similar but distinct measurements of this quantity, relative to the total kinetic energy in the simulations. Using the SSA method, we observe a growing amount of turbulent kinetic energy relative to the total kinetic energy from the onset of convection, whereas the LSA and spectral methods find a somewhat constant (and perhaps even diminishing) amount of turbulence over the same period. The

11

SSA method clearly distinguishes between successful and failing supernovae, whereas the LSA and spectral methods do not show a distinction. Further, maps of the specific turbulent kinetic energy using the SSA method are seen to be dominated by the convective plumes, whereas maps made using the LSA method more closely match the enstrophy, another metric of turbulence.

5. The Turbulent and Effective Adiabatic Index

We can now address the question of how the turbulence alters the fluid properties, and how one's conclusions about the effect of turbulence depend upon the definition. The quantities we focus upon are the adiabatic indices: the turbulent adiabatic index and the effective adiabatic index. The turbulent adiabatic tensor is defined as

$$(\gamma_{\text{turb}})_{ij} = 1 + \frac{R_{ij}}{\rho \, e_{\text{turb}}}, \qquad (24)$$

where R_{ij} is the ijth element of the Reynolds stress tensor. For the LSA and SSA, we define R_{ij} as $R_{ij} = \rho \, (v_i - \langle \boldsymbol{v} \rangle_i) \, (v_j - \langle \boldsymbol{v} \rangle_j)$, where, again, $\langle \boldsymbol{v} \rangle$ is the expectation value of the fluid velocity, and $\rho \, e_{\text{turb}}$ is the turbulent kinetic energy density. As discussed in Section 4.2, we can recover the turbulent velocity field, and thus the Reynolds stress tensor, for the spectral method as follows. We compute R_{ij} by Fourier transforming the velocity $\boldsymbol{v}$, setting the amplitude of all Fourier modes to zero for all wavenumbers $k \leqslant k_{\text{min}}$, then transforming back to real space to produce the velocity field $\boldsymbol{u}$. We then define R_{ij} as $R_{ij} = \rho \, u_i u_j$. Due to its effect upon the shock radius, the most important component of the tensor is the $ij = rr$ element; therefore, we will refer to $(\gamma_{\text{turb}})_{rr}$ as the turbulent adiabatic index γ_{turb}.

For well-developed isotropic turbulence, one expects each diagonal element (such as rr) of the tensor $(\gamma_{\text{turb}})_{ij}$ to have a triangular distribution. If the turbulence is anisotropic such that the distribution of $(\gamma_{\text{turb}})_{rr}$ is the same as the distribution of the sum $(\gamma_{\text{turb}})_{\theta\theta} + (\gamma_{\text{turb}})_{\phi\phi}$—as has been found in the simulations reported in J. C. Dolence et al. (2013)—we would expect γ_{turb} to have a uniform distribution (see the Appendix for a detailed derivation of these expectations). For the case of nonturbulent, bulk flow in the radial direction (either inward or outward), γ_{turb} should have a distribution that peaks toward $\gamma_{\text{turb}} = 3$ when using the SSA method. This last expectation arises because, for a location in the bulk flow, $\boldsymbol{v}$ will point approximately radially inward (for a downflow) or outward (for a convective plume). The combination of flows in both directions has the consequence that the average radial velocity $\langle v_r \rangle$ will point inward (mass is still accreting onto the PNS even if convection is occurring) but $\langle v_r \rangle$ will be smaller than the velocity of the fluid in the downflows. This has the effect that the Reynolds tensor element R_{rr} will typically be larger than the elements $R_{\theta\theta}$ and $R_{\phi\phi}$. Given a larger R_{rr}, we anticipate that, in the SSA method, our values of γ_{turb} will be pushed upward toward 3. In contrast, for the LSA method, the velocity of a given fluid element relative to the local average velocity would be closer to random than for the SSA, regardless of the relative size of the average fluid velocity $\langle \boldsymbol{v} \rangle$ and the deviation from the average $\boldsymbol{v} - \langle \boldsymbol{v} \rangle$. Thus, we expect the value of γ_{turb} for fluid elements in a bulk flow will not have the same bias toward $\gamma_{\text{turb}} = 3$ when using the LSA method. Similarly, when using the spectral method to compute γ_{turb}, we should also find values for γ_{turb} in fluid with bulk flow

that are also not biased toward $\gamma_{\text{turb}} = 3$, because this method removes the large-scale bulk flow component and retains only the small-scale fluid motion.

In Figure 11, we show a 2D slice of the turbulent adiabatic index γ_{turb} we obtain in each grid zone, and their histograms at the $t_{\text{pb}} = 150$ ms, using the SSA method (top panels), the LSA method (middle panels), and the spectral method (bottom panels) for the s15, s20, and s27 simulations. The number of bins in every histogram is determined by Sturges's rule (H. A. Sturges 1926). Again, the different methods for defining the turbulence lead to distinct spatial maps. In the spatial distribution of the LSA and spectral methods, the structures are of smaller scale, whereas when we use the SSA method, we observe large regions where the adiabatic index has a value $\gamma_{\text{turb}} \geqslant 2$. The histograms of the adiabatic index for the fluid in the gain region are seen to be very similar when using either the LSA or spectral methods, while the SSA is different. In particular, the distributions for the SSA method have a more pronounced peak toward $\gamma_{\text{turb}} = 3$ compared with the LSA and spectral methods. The histograms of γ_{turb} are consistent with the idea that the fluid in the gain region can be divided into three components: the fluid that has well-developed, isotropic turbulence, the fluid that has anisotropic turbulence, and the fluid that is only moderately turbulent and has a bulk flow. Each of these components of the fluid in the gain region result in different pieces of the distribution of γ_{turb} in the gain region; e.g., a triangular distribution for γ_{turb} in the case of isotropic turbulence or a uniform distribution for γ_{turb} for anisotropic turbulence. For the moderately turbulent component, the distribution for γ_{turb} is peaked toward $\gamma_{\text{turb}} = 3$ when using the SSA; for the LSA or spectral methods, the distribution of γ_{turb} will be more similar to the distribution of the other two fluid components.

The different components of the fluid can be seen more clearly if we select small patches of the gain region. We select two 50 km square patches in each simulation, one with high enstrophy and the other with low enstrophy. The patches we select and the histograms of γ_{turb} for these patches are shown in Figures 12 and 13. First, the high-enstrophy regions in Figure 12 demonstrate that all the methods for measuring the turbulence give similar distributions of γ_{turb} in regions of high enstrophy, albeit with a tendency toward larger γ_{turb} from the SSA method. Conversely, Figure 13 demonstrates that, in regions of low enstrophy, the different methods yield very different distributions of γ_{turb}.

The effect of turbulence upon the fluid and explosion, if any, needs to be compared with other sources of energy and pressure in the fluid. For this purpose, we can define an effective adiabatic index to be

$$\gamma_{\text{eff}} = 1 + \frac{R_{rr} + P_{\text{thermal}}}{E_{\text{turb}} + E_{\text{thermal}}}$$
$$= \left(\frac{\alpha}{1 + \alpha} \right) \gamma_{\text{turb}} + \left(\frac{1}{1 + \alpha} \right) \gamma_{\text{thermal}}, \qquad (25)$$

where $E_{\text{thermal}} = \rho \, e_{\text{thermal}}$ and P_{thermal} represent the specific thermal energy and pressure, $\gamma_{\text{thermal}} = 1 + P_{\text{thermal}}/(\rho \, e_{\text{thermal}})$, and $\alpha = e_{\text{turb}}/e_{\text{thermal}}$. In Figure 14, we show histograms of γ_{thermal} and γ_{eff} for the gain region from the same snapshots at 150 ms post-bounce of the exploding simulations using the three different turbulence calculation methods. The thermal adiabatic index is approximately $\gamma_{\text{thermal}} = 1.43$ for all fluid within the
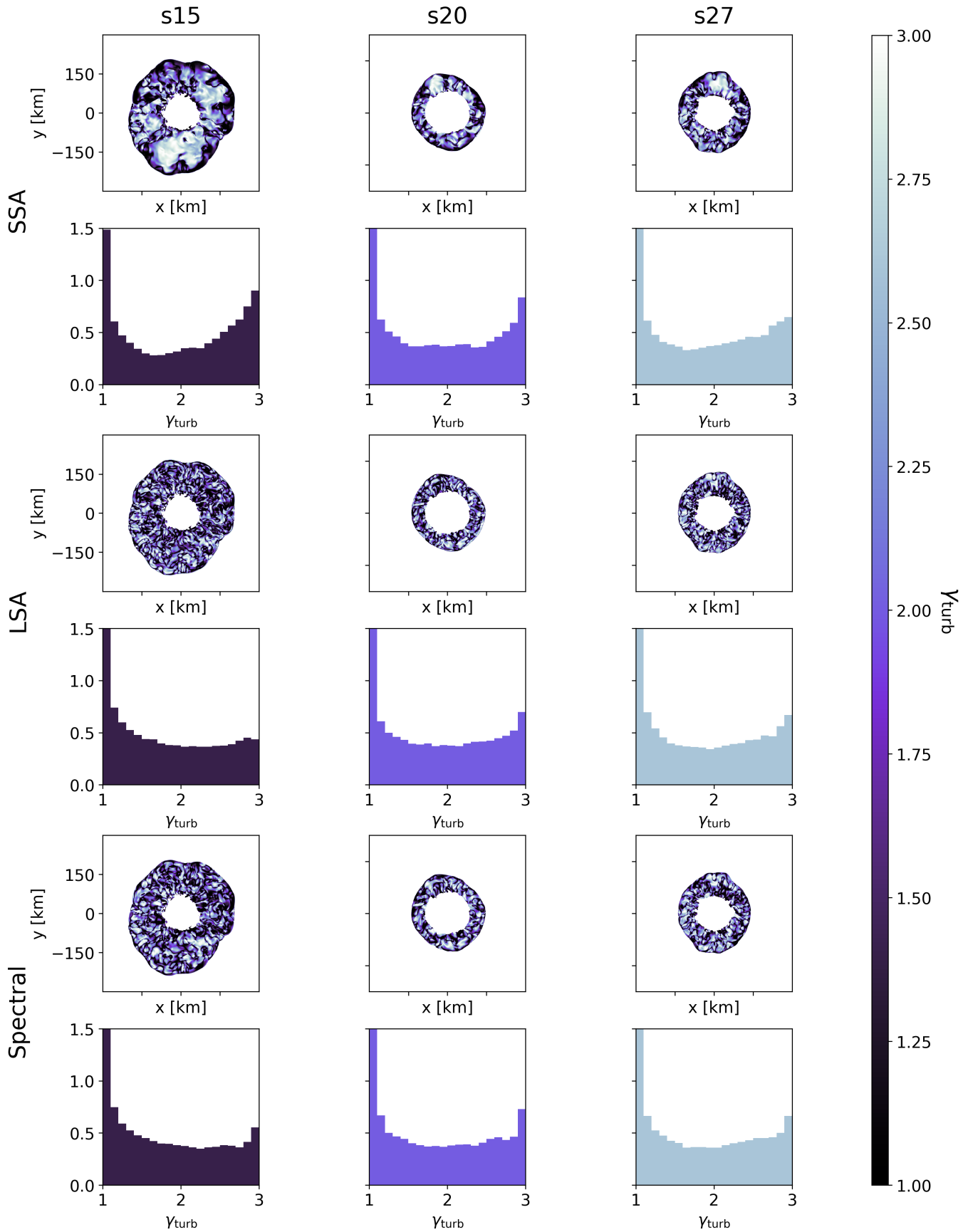
Figure 11. Top: maps in the *xy*-plane and histograms of the turbulent adiabatic index γ_{turb} in the gain region for the s15, s20, and s27 simulations using SSA (top), LSA (middle), and the spectral method (bottom row).
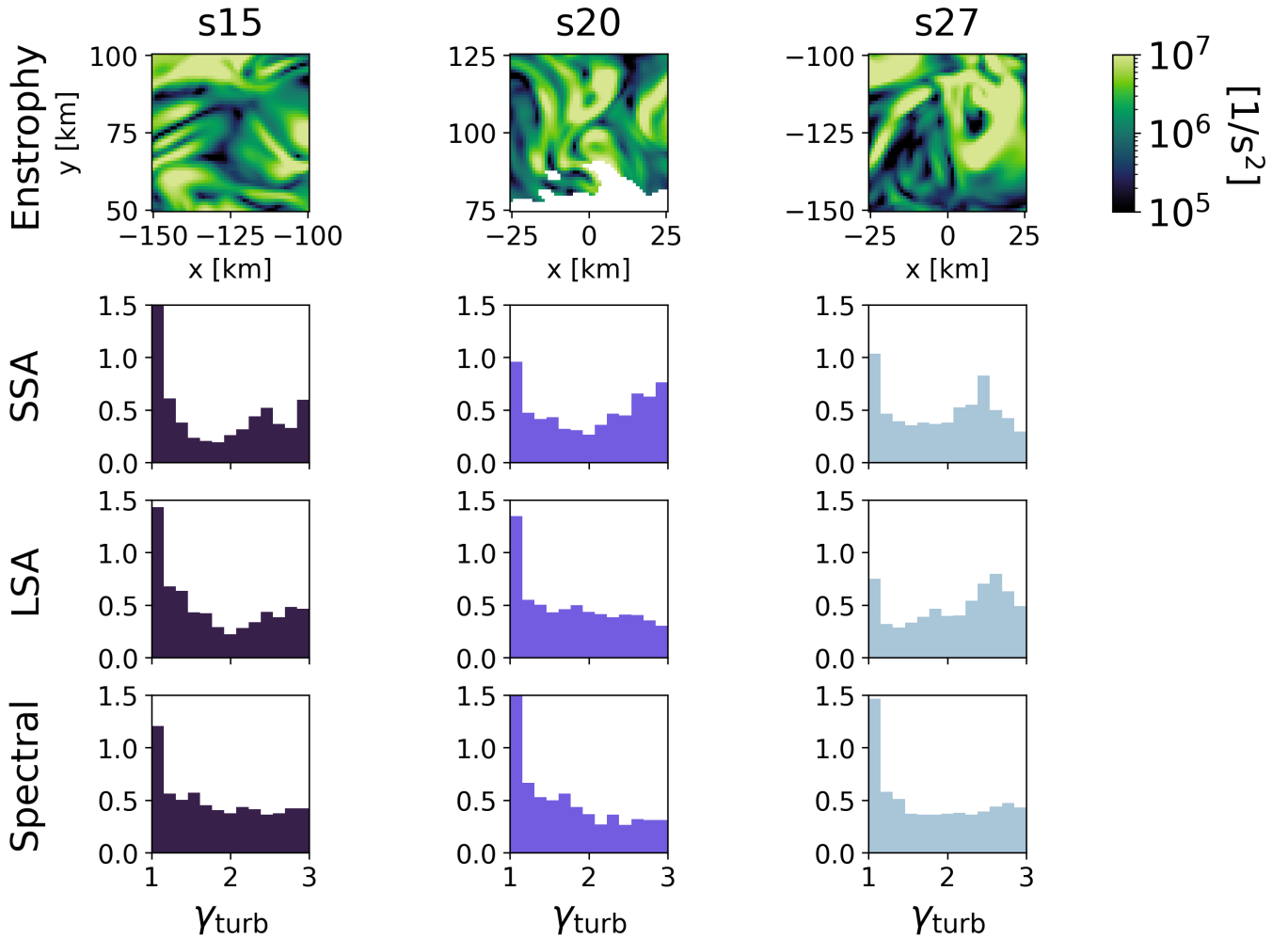
Figure 12. Enstrophy map in the *xy*-plane (top row) and distribution of γ_{turb} for a high-enstrophy patch in the gain region. The γ_{turb} are computed using the SSA method (second row), the LSA method (third row), and the spectral method (bottom row).

gain region at this time. When we add the contribution from turbulence and compute γ_{eff}, the peak at 1.43 is retained but its width increases. When we use the LSA or spectral methods, the broadening is smaller than when we use the SSA method. The addition of the turbulence shifts the average value of γ_{eff} upward, and the average γ_{eff} values for these snapshots are shown in Table 1. Whatever method we use to define the turbulence, the shift of γ_{eff} from $\gamma_{thermal}$ is not large; for the successful explosions, γ_{eff} is larger than $\gamma_{thermal}$ by, at most, 5%, as seen in Table 1. Notably, the largest shifts come from the SSA method, while similar but smaller shifts come from the LSA and spectral methods. This further confirms the notion that the methods can suggest different amounts of importance of turbulence relative to other physics.

Finally, in Figures 15 and 16, we show the evolution of the average thermal and effective adiabatic indices for the entire gain region as a function of the post-bounce time. As the fluid in the gain region is heated, its thermal adiabatic index gradually decreases due to a greater proportion of relativistic material to nonrelativistic material. The decrease is not large; only 3% over the 100 ms period shown. The evolution of γ_{eff} over this same period, on the other hand, depends upon the method used to define turbulence, as shown in Figure 15. In all

three successful explosions, the SSA method yields an average γ_{eff} that is larger than for the other two definitions of turbulence, and it remains consistently between 1.48 and 1.5. This behavior is just as we saw at the single time point above, but we can now generalize to more of the simulation as a function of post-bounce time. In contrast, the LSA and spectral methods for computing the turbulence yield average γ_{eff} values that gradually decrease with time, although by only ∼4%.

6. Summary, Conclusions, and Discussion

In this paper, we have investigated the question of how different definitions of the turbulence alters one's conclusions about the effect of turbulence in supernova simulations. We have undertaken four simulations using four progenitors, and used three different methods for computing the turbulence. We find that how the turbulence is defined alters the amount of measured turbulent kinetic energy in the gain region. The SSA method consistently yields values for the turbulent kinetic energy that are larger than the values obtained with the LSA and spectral methods. The differences are only partly explained away by the choices one has to make for the averaging volume scale in the LSA method and the minimum wavenumber in the spectral method. The remaining difference is indicative of the fundamental differences of the definitions.
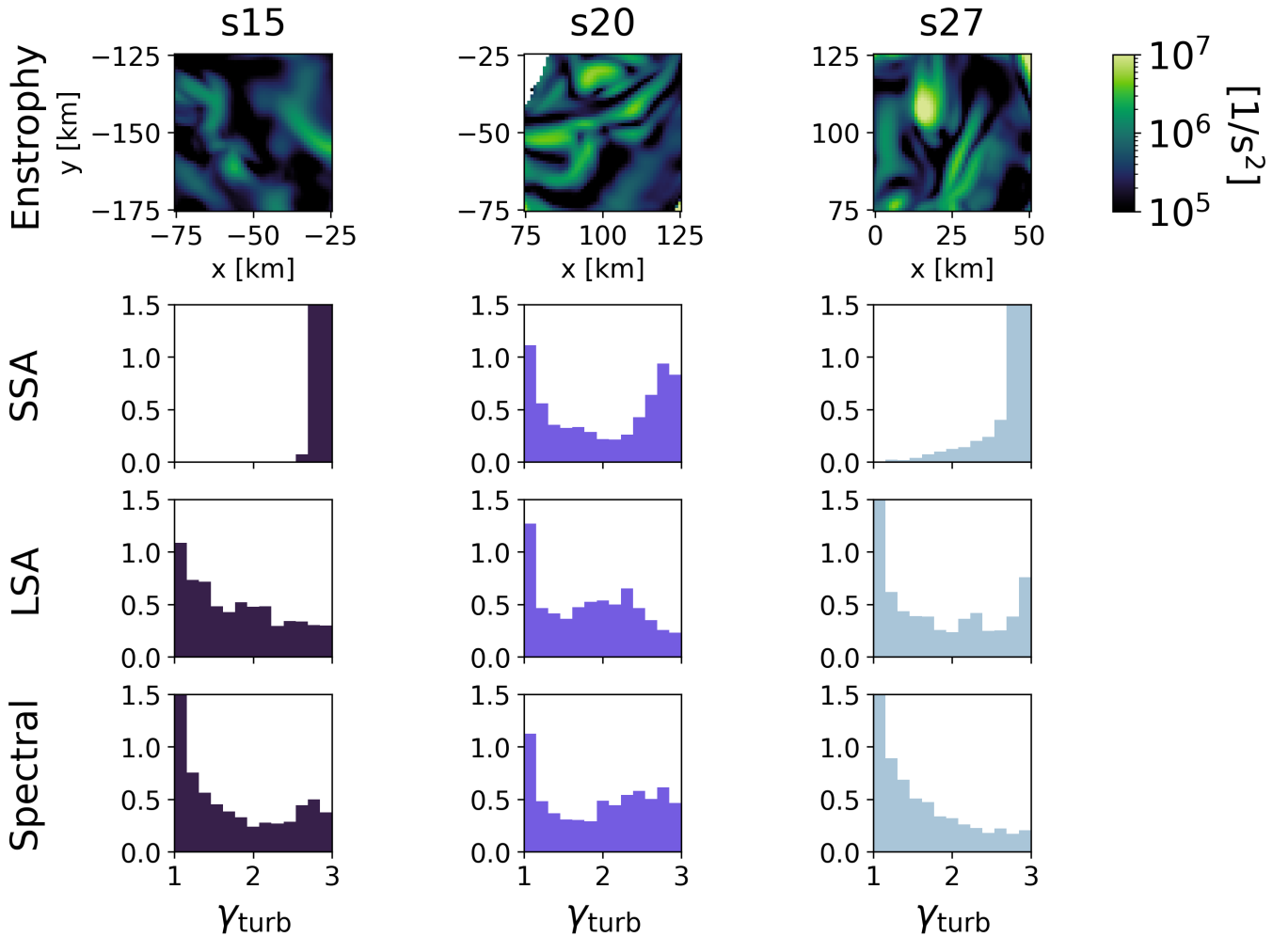
Figure 13. Enstrophy map in the *xy*-plane (top row) and distribution of $\gamma_{\rm turb}$ for a low-enstrophy patch in the gain region. The $\gamma_{\rm turb}$ are computed using the SSA method (second row), the LSA method (third row), and the spectral method (bottom row).

These fundamental differences are seen most clearly in Figure 8, which shows how the ratio of the turbulent kinetic energy to total kinetic energy in the gain region evolves with time. The SSA method finds a consistently larger ratio of the energies for successful explosions, and the ratio tends to grow as a function of post-bounce time. Using the SSA, one would conclude that the presence of turbulence correlates with the success of the explosion. In contrast, the ratios of energies calculated using the LSA and spectral methods are similar for both successful *and* unsuccessful explosions. Using these methods, one would conclude that the presence of turbulence does not correlate with the success of the supernova. This divergence of conclusions indicates that the different methods of measuring the turbulence are actually not measuring the same thing.

To determine which method, if any, is a better measure of the turbulence we compared maps of the specific turbulent kinetic energy with maps for the enstrophy, a quantity that is often associated with the presence of turbulence. The comparison revealed that the LSA and spectral methods produce maps that are more similar to the enstrophy than the SSA method.

Finally, we examined the effect of turbulence upon the fluid by computing the turbulent and effective adiabatic indices.

Maps of the turbulent adiabatic index calculated using the SSA show larger coherent regions with $\gamma_{\rm turb} > 2$ compared to those produced by the LSA and spectral methods. These large regions of high $\gamma_{\rm turb}$ alter the distributions of this adiabatic index, producing a peak in the distribution toward the maximum value $\gamma_{\rm turb} = 3$. The net effect is to shift the average turbulent adiabatic index in the gain region upward by a larger amount when using the SSA definition compared to the shift when using either of the other two definitions.

The contribution of turbulence to the explosion can be measured by computing the effective adiabatic index $\gamma_{\rm eff}$. All definitions of turbulence shift the average $\gamma_{\rm eff}$ upward. However, the shift is more pronounced when we use the SSA method compared to the LSA and spectral definitions. Furthermore, the average $\gamma_{\rm eff}$ in the gain region remains approximately constant when we use the SSA. In contrast, when we use the LSA or spectral definitions, the average $\gamma_{\rm eff}$ decreases with time. These findings once again demonstrate that the method selected for defining the turbulence changes the interpretation of the impact of turbulence as a function of post-bounce time.

When assessing the impact of turbulence on the evolution of CCSNe, it is necessary to understand the strengths and limitations of the method used to measure it. We conclude
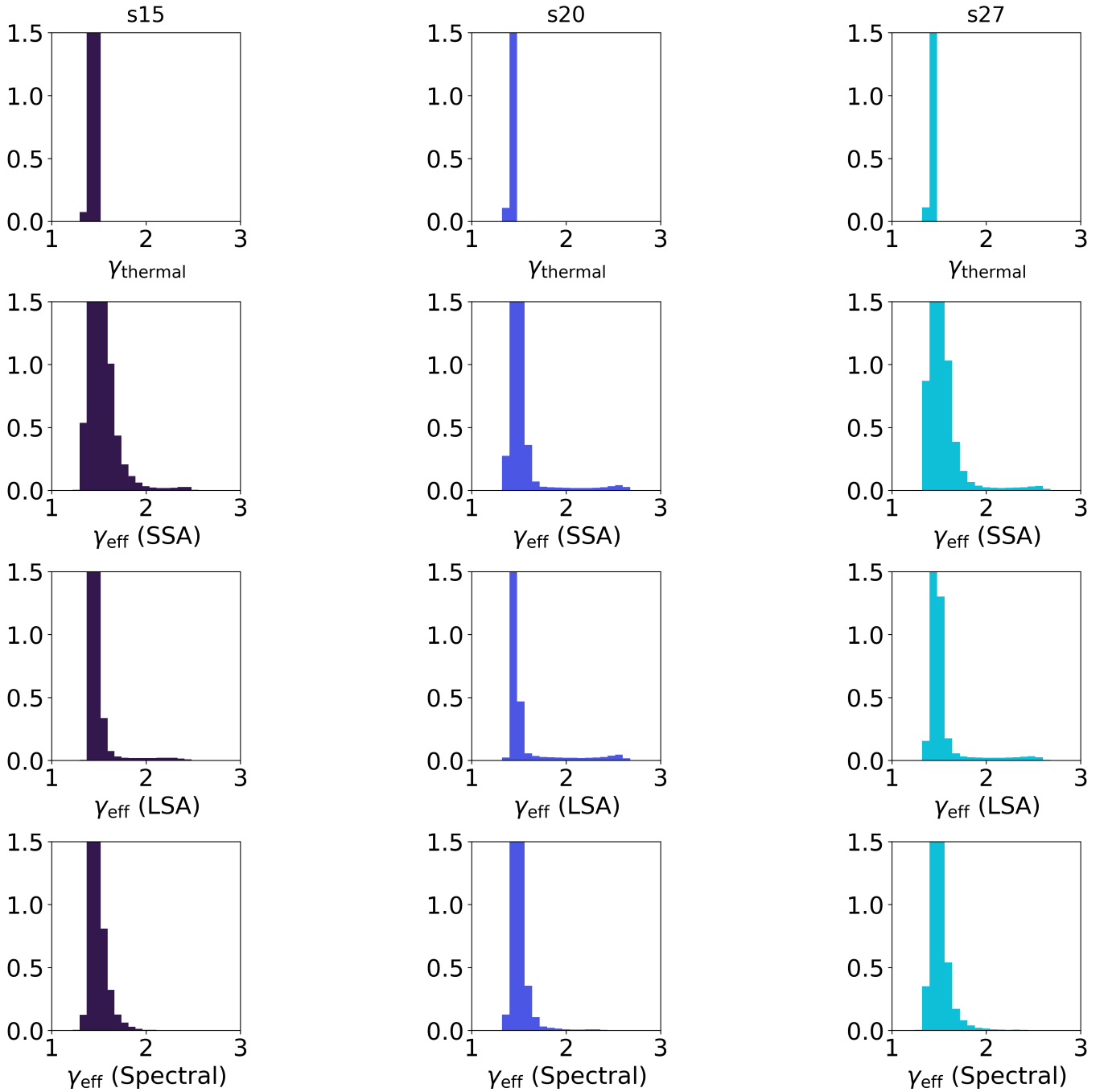
Figure 14. Distribution of the thermal adiabatic index γ_{thermal} (top) and the effective adiabatic index γ_{eff} using the SSA (second row), LSA (third row), and spectral method (bottom).

from our study that the SSA method for defining the turbulence is not as accurate of a measure of this quantity as the LSA and spectral methods. The LSA and spectral methods are more consistent with each other *and* with the distribution of enstrophy in the simulations. The SSA yields a turbulent kinetic energy that is dominated by the upflowing convective plumes, not actual turbulence. However, the LSA and spectral definitions are not free of systematic problems. For example, using the LSA for the fluid in the vicinity of counterflows means there is a great deal of cancellation of momentum within the averaging volume, which tends to yield low average velocities and thus larger contributions to the turbulent kinetic energy. Further, both methods require one to define an additional parameter, and we have found that the measure of the turbulent kinetic energy is not independent of this choice. Thus, the LSA and spectral methods suffer from an element of subjectivity that the SSA does not share. Nevertheless, the systematic issues of the LSA and spectral definitions appear to not have as great an effect upon turbulent kinetic energy as convection has upon the SSA.

While the LSA and spectral methods correlate more closely to the often-used turbulence tool of enstrophy, the quantity measured by the SSA method is clearly useful, because it correlates with the success of the explosion. Since the

Table 1
Average Thermal, Turbulent, and Effective Adiabatic Indices, and Difference (Δ) of $\overline{\gamma}_{\text{eff}}$ Relative to $\overline{\gamma}_{\text{Thermal}}$

Simulation	$\overline{\gamma}_{\text{thermal}}$	$\overline{\gamma}_{\text{turb}}$			$\overline{\gamma}_{\text{eff}}$			Δ		
		SSA	LSA	Spectral	SSA	LSA	Spectral	SSA	LSA	Spectral
s15	1.4271	1.9985	1.8171	1.8203	1.4961	1.4481	1.4522	0.0483	0.0147	0.0176
s20	1.4364	1.9334	1.9084	1.8986	1.4777	1.4635	1.4616	0.0288	0.0189	0.0175
s27	1.4326	1.9362	1.9044	1.8998	1.4933	1.4630	1.4623	0.0424	0.0212	0.0207

Note. $\Delta = (\overline{\gamma}_{\text{thermal}} - \overline{\gamma}_{\text{eff,X}})/\overline{\gamma}_{\text{thermal}}$ where X represents SSA, LSA, or spectral, respectively.
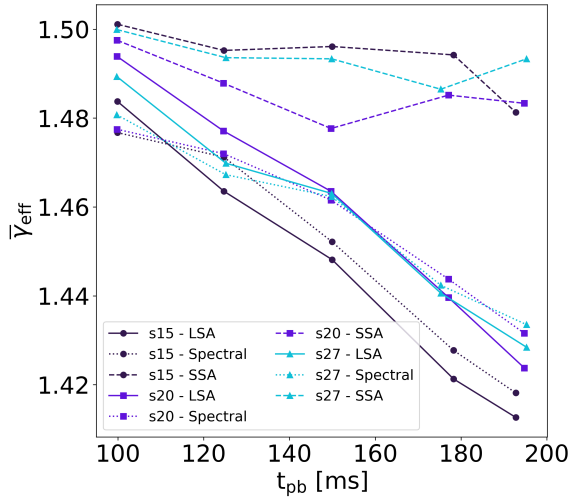
Figure 15. Average effective adiabatic index $\overline{\gamma}_{\text{eff}}$ in the gain region as a function of post-bounce time using the LSA (solid line), SSA (dashed line), and spectral methods (dotted line) for the s15, s20, and s27 simulations.
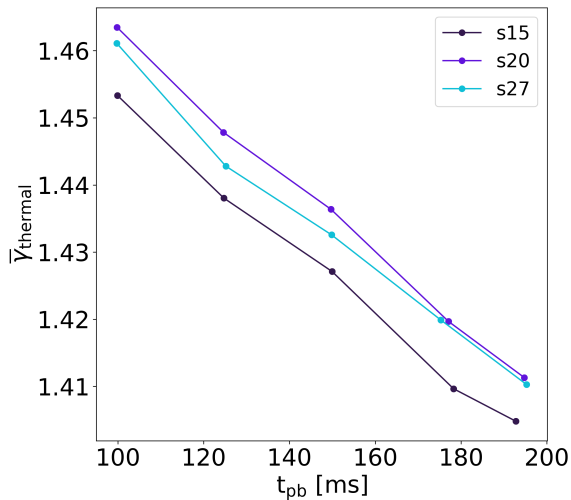
Figure 16. Average thermal adaibatic index $\overline{\gamma}_{\text{thermal}}$ in the gain region as a function of post-bounce time for the s15, s20, and s27 simulations.

turbulent kinetic energy computed using the SSA is dominated by convective plumes, the correlation suggests that the transition to explosion is because the kinetic energy in the gain region is increasingly directed toward countering the ram pressure of the infalling material. Since the turbulent kinetic energy computed using the SSA is dominated by convective plumes, the correlation suggests that the SSA is more likely to be tracking convection than turbulence. While there are a multitude of mechanisms, such as neutrino heating and deleptonization, contributing to the convection, the connection between SSA and explosion can be more accurately attributed to the necessity for convection for a supernova to explode

Appendix
The Distribution of the Turbulent Adiabatic Index in Well-developed Turbulence

The elements of the adiabatic index tensor for turbulence are defined to be

$$(\gamma_{\text{turb}})_{ij} = 1 + \frac{R_{ij}}{E_{\text{turb}}}, \tag{A1}$$

with R_{ij} the ijth element of the Reynolds stress tensor given by $R_{ij} = \rho \, (v_i - \langle \boldsymbol{v} \rangle_i) \, (v_j - \langle \boldsymbol{v} \rangle_j)$, $\langle \boldsymbol{v} \rangle$ is the expectation value of the fluid velocity, and E_{turb} is the turbulent kinetic energy $E_{\text{turb}} = \rho \, |\boldsymbol{v} - \langle \boldsymbol{v} \rangle|^2 / 2$. For our derivation of the distribution

of the adiabatic index in well-developed turbulence, it does not matter how $\langle v \rangle$ is defined. The diagonal elements of the Reynolds stress tensor are non-negative, and from the definition of the Reynolds stress tensor, we see that

$$2\,E_{\text{turb}} = \sum_i R_{ii}. \tag{A2}$$

Thus, the three diagonal components of the Reynold's stress tensor are not independent: they are constrained, and the constraint defines a simplex in the space of R_{rr}, $R_{\theta\theta}$, and $R_{\phi\phi}$ (using spherical coordinate labels for the diagonal elements of R_{ij}).

A.1. Isotropic Turbulence

In isotropic turbulence, the values for the diagonal elements of the Reynold's stress tensor at a given location in the fluid may be regarded as random and equally likely, i.e., each diagonal element of the stress tensor has the same probability distribution. This means that, for a fixed total energy E_{turb}, the infinitesimal probability $dP(R_{rr}, R_{\theta\theta}, R_{\phi\phi})$ of finding the diagonal elements of the stress tensor in the ranges R_{rr} to $R_{rr} + dR_{rr}$, $R_{\theta\theta}$ to $R_{\theta\theta} + dR_{\theta\theta}$, and $R_{\phi\phi}$ to $R_{\phi\phi} + dR_{\phi\phi}$, is uniform across the surface of the simplex and so proportional to the surface element $dA = \delta(2\,E_{\text{turb}} - R_{rr} - R_{\theta\theta} - R_{\phi\phi})\,dR_{rr}\,dR_{\theta\theta}\,dR_{\phi\phi}$ of the simplex. Thus, we can write the probability of a given set of diagonal elements as

$$dP(R_{rr}, R_{\theta\theta}, R_{\phi\phi}) \propto \delta(2\,E_{\text{turb}} - R_{rr} - R_{\theta\theta} - R_{\phi\phi}) \\ \times dR_{rr}\,dR_{\theta\theta}\,dR_{\phi\phi}. \tag{A3}$$

To find the distribution of any one diagonal element, e.g., R_{rr}, we integrate this probability distribution over the other two diagonal elements, i.e.,

$$\frac{dP(R_{rr})}{dR_{rr}} = C \int_0^{2\,E_{\text{turb}}} \int_0^{2\,E_{\text{turb}}} \delta(2\,E_{\text{turb}} \\ - R_{rr} - R_{\theta\theta} - R_{\phi\phi})\,dR_{\theta\theta}\,dR_{\phi\phi}. \tag{A4}$$

where C is a normalization constant. To evaluate the integral, we first insert two Heaviside step functions so that we can change the limits of the integration for one variable, e.g., $R_{\phi\phi}$, and write

$$\frac{dP(R_{rr})}{dR_{rr}} = C \int_0^{2\,E_{\text{turb}}} \int_{-\infty}^{\infty} \delta(2\,E_{\text{turb}} - R_{rr} - R_{\theta\theta} - R_{\phi\phi}) \\ \times \Theta(2\,E_{\text{turb}} - R_{\phi\phi})\,\Theta(R_{\phi\phi})\,dR_{\theta\theta}\,dR_{\phi\phi}. \tag{A5}$$

From the integral over $R_{\phi\phi}$, we obtain

$$\frac{dP(R_{rr})}{dR_{rr}} = C \int_0^{2\,E_{\text{turb}}} \Theta(2\,E_{\text{turb}} - R_{rr} - R_{\theta\theta}) \\ \times \Theta(R_{rr} + R_{\theta\theta})\,dR_{\theta\theta}, \tag{A6}$$

and now we can remove the step functions by changing the limits of the remaining integral over $R_{\theta\theta}$ to give

$$\frac{dP(R_{rr})}{dR_{rr}} = C \int_0^{2\,E_{\text{turb}} - R_{rr}} dR_{\theta\theta}. \tag{A7}$$

The integral is now trivial, and after normalizing, we find

$$\frac{dP(R_{rr})}{dR_{rr}} = \frac{1}{E_{\text{turb}}}\left(1 - \frac{R_{rr}}{2\,E_{\text{turb}}}\right). \tag{A8}$$

This is a triangular distribution for R_{rr}. Now that we know the distribution of R_{rr}, we see that the distribution for γ_{rr} (or any other diagonal element of the tensor) is also a triangular distribution,

$$\frac{dP(\gamma_{rr})}{d\gamma_{rr}} = \frac{(3 - \gamma_{rr})}{2}, \tag{A9}$$

with a range $1 \leqslant \gamma_{rr} \leqslant 3$. The average adiabatic index is $\langle \gamma_{rr} \rangle = 5/3$, which matches the well-known result of the adiabatic index of isotropic turbulence (D. Radice et al. 2018).

A.2. Anisotropic Turbulence

For anisotropic turbulence, one of the diagonal components of the Reynolds stress has a distribution different from the other two. In many models of anisotropic turbulence, e.g., J. W. Murphy et al. (2013), the distribution of the biased component is equal to the distribution of the sum of the other two components. Defining $R_{tt} = R_{\theta\theta} + R_{\phi\phi}$, the probability $dP(R_{rr}, R_{tt})$ of finding the elements of the stress tensor in the ranges R_{rr} to $R_{rr} + dR_{rr}$ and R_{tt} to $R_{tt} + dR_{tt}$, is uniform across the line $2E_{\text{turb}} = R_{rr} + R_{tt}$, and therefore proportional to the line element $d\ell = \delta(2E_{\text{turb}} - R_{rr} - R_{tt})dR_{rr}\,dR_{tt}$. We can proceed exactly as before to integrate over R_{tt} to determine the distribution of R_{rr}. We find

$$\frac{dP(R_{rr})}{dR_{rr}} = \frac{1}{2\,E_{\text{turb}}}\,\Theta(R_{rr})\,\Theta(2\,E_{\text{turb}} - R_{rr}), \tag{A10}$$

which is a uniform distribution. Thus, $\gamma_{rr} = 1 + R_{rr}/E_{\text{turb}}$ is also uniform and equal to

$$\frac{dP(\gamma_{rr})}{d\gamma_{rr}} = \frac{1}{2}\,\Theta(\gamma_{rr} - 1)\,\Theta(3 - \gamma_{rr}). \tag{A11}$$

From this result, we recover the result that, for anisotropic turbulence, the average adiabatic index is $\langle \gamma_{rr} \rangle = 2$ (D. Radice et al. 2018).

ORCID iDs

David Calvert ◉ https://orcid.org/0009-0000-5846-5984
Michael Redle ◉ https://orcid.org/0000-0002-4099-2978
Bibek Gautam ◉ https://orcid.org/0000-0002-3211-3427
Charles J. Stapleford ◉ https://orcid.org/0000-0002-5667-7577
Carla Fröhlich ◉ https://orcid.org/0000-0003-0191-2477
James P. Kneller ◉ https://orcid.org/0000-0002-3502-3830
Matthias Liebendorfer ◉ https://orcid.org/0000-0001-8523-9528

References

Abdikamalov, E., Ott, C. D., Radice, D., et al. 2015, ApJ, 808, 70
Adrian, R. J., Christensen, K. T., & Liu, Z. C. 2000, ExFl, 29, 275
Andresen, H., Müller, B., Müller, E., & Janka, H. T. 2017, MNRAS, 468, 2032
Astropy Collaboration, Price-Whelan, A. M., Lim, P. L., et al. 2022, ApJ, 935, 167
Astropy Collaboration, Price-Whelan, A. M., Sipöcz, B. M., et al. 2018, AJ, 156, 123
Astropy Collaboration, Robitaille, T. P., Tollerud, E. J., et al. 2013, A&A, 558, A33
Bethe, H. A., & Wilson, J. R. 1985, ApJ, 295, 14
Blondin, J. M., & Mezzacappa, A. 2007, Natur, 445, 58
Blondin, J. M., Mezzacappa, A., & DeMarino, C. 2003, ApJ, 584, 971
Bloom, J. S., Kulkarni, S. R., Djorgovski, S. G., et al. 1999, Natur, 401, 453

Boccioli, L., & Roberti, L. 2024, Univ, 10, 148
Bollig, R., Yadav, N., Kresse, D., et al. 2021, ApJ, 915, 28
Bruenn, S. W. 1985, ApJS, 58, 771
Bruenn, S. W., Lentz, E. J., Hix, W. R., et al. 2016, ApJ, 818, 123
Buras, R., Janka, H. T., Rampp, M., & Kifonidis, K. 2006, A&A, 457, 281
Burrows, A., Hayes, J., & Fryxell, B. A. 1995, ApJ, 450, 830
Burrows, A., & Lattimer, J. M. 1986, ApJ, 307, 178
Burrows, A., & Vartanyan, D. 2021, Natur, 589, 29
Cabezón, R. M., Pan, K.-C., Liebendörfer, M., et al. 2018, A&A, 619, A118
Casanova, J., Endeve, E., Lentz, E. J., et al. 2020, PhyS, 95, 064005
Couch, S. M. 2017, RSPTA, 375, 20160271
Couch, S. M., & O'Connor, E. P. 2014, ApJ, 785, 123
Couch, S. M., & Ott, C. D. 2013, ApJL, 778, L7
Couch, S. M., & Ott, C. D. 2015, ApJ, 799, 5
Couch, S. M., Warren, M. L., & O'Connor, E. P. 2020, ApJ, 890, 127
Curtis, S., Ebinger, K., Fröhlich, C., et al. 2019, ApJ, 870, 2
Dobler, W., Haugen, N. E., Yousef, T. A., & Brandenburg, A. 2003, PhRvE, 68, 026304
Dolence, J. C., Burrows, A., Murphy, J. W., & Nordhaus, J. 2013, ApJ, 765, 110
Duncan, R. C., & Thompson, C. 1992, ApJL, 392, L9
Ebinger, K., Curtis, S., Fröhlich, C., et al. 2019, ApJ, 870, 1
Endeve, E., Cardall, C. Y., Budiardja, R. D., Mezzacappa, A., & Blondin, J. M. 2013, PhST, 155, 014022
Endeve, E., Cardall, C. Y., Budiardja, R. D., et al. 2012, ApJ, 751, 26
Ertl, T., Janka, H. T., Woosley, S. E., Sukhbold, T., & Ugliano, M. 2016, ApJ, 818, 124
Falkovich, G. 1994, PhFl, 6, 1411
Fernández, R. 2012, ApJ, 749, 142
Fernández, R., Müller, B., Foglizzo, T., & Janka, H.-T. 2014, MNRAS, 440, 2763
Glas, R., Just, O., Janka, H. T., & Obergaulinger, M. 2019, ApJ, 873, 45
Handy, T., Plewa, T., & Odrzywołek, A. 2014, ApJ, 783, 125
Hanke, F., Marek, A., Müller, B., & Janka, H.-T. 2012, ApJ, 755, 138
Hanke, F., Müller, B., Wongwathanarat, A., Marek, A., & Janka, H.-T. 2013, ApJ, 770, 66
Harris, C. R., Millman, K. J., van der Walt, S. J., et al. 2020, Natur, 585, 357
Hunter, J. D. 2007, CSE, 9, 90
Janka, H. T. 2001, A&A, 368, 527
Janka, H.-T. 2017, Neutrino-Driven Explosions, in Handbook of Supernovae, ed. A. Alsabti & P. Murdin (Springer), 1095
Janka, H. T. 2025, ARNPS, 75, 425
Janka, H. T., & Keil, W. 1998, Supernovae and Cosmology, in in Proc. Colloquium Held in Honor of Gustav Andreas Tammann on the Occasion of his 65th birthday, ed. L. Labhardt, B. Binggeli, & R. Buser (Astronomisches Institut), 7
Janka, H. T., Langanke, K., Marek, A., Martínez-Pinedo, G., & Müller, B. 2007, PhR, 442, 38
Jin, S., & Xin, Z. 1995, Communications on Pure and Applied Mathematics, 48, 235
Käppeli, R., Whitehouse, S. C., Scheidegger, S., Pen, U.-L., & Liebendörfer, M. 2011, ApJS, 195, 20
Kaspi, V. M., & Beloborodov, A. M. 2017, ARA&A, 55, 261
Katul, G. G., Manes, C., Porporato, A., Bou-Zeid, E., & Chamecki, M. 2015, PhRvE, 92, 033009
Kuroda, T., Arcones, A., Takiwaki, T., & Kotake, K. 2020, ApJ, 896, 102
Lattimer, J. M., & Swesty, F. D. 1991, NuPhA, 535, 331
Liebendörfer, M., Messer, O. E. B., Mezzacappa, A., et al. 2004, ApJS, 150, 263

Liebendörfer, M., Whitehouse, S. C., & Fischer, T. 2009, ApJ, 698, 1174
Marek, A., Dimmelmeier, H., Janka, H., Müller, E., & Buras, R. 2006, A&A, 445, 273
Matsumoto, J., Takiwaki, T., & Kotake, K. 2024, MNRAS, 528, L96
Melson, T., Janka, H.-T., Bollig, R., et al. 2015a, ApJL, 808, L42
Melson, T., Janka, H.-T., & Marek, A. 2015b, ApJL, 801, L24
Mereghetti, S., Pons, J. A., & Melatos, A. 2015, SSRv, 191, 315
Mezzacappa, A., Liebendörfer, M., Messer, O. E., et al. 2001, PhRvL, 86, 1935
Mezzacappa, A., Lentz, E. J., Bruenn, S. W., et al. 2015, arXiv:1507.05680
Müller, B., & Varma, V. 2020, MNRAS, 498, L109
Murphy, J. W., & Burrows, A. 2008, ApJ, 688, 1159
Murphy, J. W., Dolence, J. C., & Burrows, A. 2013, ApJ, 771, 52
Murphy, J. W., & Meakin, C. 2011, ApJ, 742, 74
Nagakura, H., Burrows, A., Radice, D., & Vartanyan, D. 2019, MNRAS, 490, 4622
Nakamura, K., Takiwaki, T., & Kotake, K. 2022, MNRAS, 514, 3941
Nakamura, K., Takiwaki, T., Matsumoto, J., & Kotake, K. 2025, MNRAS, 536, 280
Nomoto, K., Maeda, K., Tanaka, M., & Suzuki, T. 2011, Ap&SS, 336, 129
Nomoto, K., Tominaga, N., Umeda, H., Kobayashi, C., & Maeda, K. 2006, NuPhA, 777, 424
Ott, C. D., Roberts, L. F., da Silva Schneider, A., et al. 2018, ApJL, 855, L3
Perego, A., Hempel, M., Fröhlich, C., et al. 2015, ApJ, 806, 275
Powell, J., & Müller, B. 2024, MNRAS, 532, 4326
Radice, D., Abdikamalov, E., Ott, C. D., et al. 2018, JPhG, 45, 053003
Radice, D., Ott, C. D., Abdikamalov, E., et al. 2016, ApJ, 820, 76
Rampp, M., & Janka, H. T. 2002, A&A, 396, 361
Ryu, D., Jones, T. W., & Frank, A. 2000, ApJ, 545, 475
Shankar, S., Mösta, P., Haas, R., & Schnetter, E. 2025, arXiv:2504.11537
Shibagaki, S., Kuroda, T., Kotake, K., Takiwaki, T., & Fischer, T. 2024, MNRAS, 531, 3732
Skinner, M. A., Burrows, A., & Dolence, J. C. 2016, ApJ, 831, 81
Smartt, S. J., Eldridge, J. J., Crockett, R. M., & Maund, J. R. 2009, MNRAS, 395, 1409
Sturges, H. A. 1926, JASA, 21, 65
Sukhbold, T., Woosley, S. E., & Heger, A. 2018, ApJ, 860, 93
Sumiyoshi, K., Yamada, S., Suzuki, H., et al. 2005, ApJ, 629, 922
Summa, A., Hanke, F., Janka, H.-T., et al. 2016, ApJ, 825, 6
Suwa, Y., Yamada, S., Takiwaki, T., & Kotake, K. 2016, ApJ, 816, 43
Sykes, B., & Müller, B. 2024, PhRvD, 111, 063042
Takiwaki, T., Kotake, K., & Foglizzo, T. 2021, MNRAS, 508, 966
Tamborra, I., Raffelt, G., Hanke, F., Janka, H.-T., & Müller, B. 2014, PhRvD, 90, 045032
Thompson, T. A., Burrows, A., & Pinto, P. A. 2003, ApJ, 592, 434
Thompson, T. A., Quataert, E., & Burrows, A. 2005, ApJ, 620, 861
Tsinober, A. 2004, An Informal Introduction to Turbulence, Vol. 63
Vartanyan, D., Burrows, A., Radice, D., Skinner, M. A., & Dolence, J. 2018, MNRAS, 477, 3091
Vartanyan, D., Burrows, A., Wang, T., Coleman, M. S. B., & White, C. J. 2023, PhRvD, 107, 103015
Vartanyan, D., Coleman, M. S. B., & Burrows, A. 2022, MNRAS, 510, 4689
Wang, L. J., Yu, H., Liu, L. D., et al. 2017, ApJ, 837, 128
Wang, T., & Burrows, A. 2024, ApJ, 962, 71
Woosley, S. E., & Bloom, J. S. 2006, ARA&A, 44, 507
Woosley, S. E., & Heger, A. 2007, PhR, 442, 269
Woosley, S. E., & Heger, A. 2015, ApJ, 810, 34
Woosley, S. E., Heger, A., & Weaver, T. A. 2002, RvMP, 74, 1015